

THEORETICAL INVESTIGATION OF THE NANOTRIBOLOGICAL  
PROPERTIES OF THE HEXAGONAL BORON NITRIDE AND GOLD  
INTERFACES

A THESIS SUBMITTED TO  
THE GRADUATE SCHOOL OF NATURAL AND APPLIED SCIENCES  
OF  
MIDDLE EAST TECHNICAL UNIVERSITY

BY

GIZEM ÖZCAN

IN PARTIAL FULFILLMENT OF THE REQUIREMENTS  
FOR  
THE DEGREE OF MASTER OF SCIENCE  
IN  
PHYSICS

JANUARY 2020



Approval of the thesis:

**THEORETICAL INVESTIGATION OF THE NANOTRIBOLOGICAL  
PROPERTIES OF THE HEXAGONAL BORON NITRIDE AND GOLD  
INTERFACES**

submitted by **GIZEM ÖZCAN** in partial fulfillment of the requirements for the degree of **Master of Science in Physics Department, Middle East Technical University** by,

Prof. Dr. Halil Kalıpçılar  
Dean, Graduate School of **Natural and Applied Sciences**

\_\_\_\_\_

Prof. Dr. Altuğ Özpineci  
Head of Department, **Physics**

\_\_\_\_\_

Assoc. Prof. Dr. Hande Toffoli  
Supervisor, **Physics, METU**

\_\_\_\_\_

**Examining Committee Members:**

Prof. Dr. Oğuz Gülseren  
Physics, Bilkent University

\_\_\_\_\_

Assoc. Prof. Dr. Hande Toffoli  
Physics, METU

\_\_\_\_\_

Prof. Dr. Mehmet Parlak  
Physics, METU

\_\_\_\_\_

Date: 24.01.2020

**I hereby declare that all information in this document has been obtained and presented in accordance with academic rules and ethical conduct. I also declare that, as required by these rules and conduct, I have fully cited and referenced all material and results that are not original to this work.**

Name, Surname: Gizem Özcan

Signature :

## **ABSTRACT**

### **THEORETICAL INVESTIGATION OF THE NANOTRIBOLOGICAL PROPERTIES OF THE HEXAGONAL BORON NITRIDE AND GOLD INTERFACES**

Özcan, Gizem

M.S., Department of Physics

Supervisor: Assoc. Prof. Dr. Hande Toffoli

January 2020, 64 pages

Frictional properties of two-dimensional structures on the nanoscale have gained importance, especially in the last decades, and a considerable amount of research is carried on to understand the interaction between their interfaces with well known lubricants. In industrial developments, these materials' interfacial properties on metals have great importance. Therefore, in this thesis, we theoretically investigated the hexagonal BN and Au(111) interface with using molecular dynamics simulation. Calculation results have shown that the friction coefficient decreases with increasing load and a noticeable dependence on temperature is observed. We observed that the nanotribology properties of these two samples highly depend on sliding velocity, orientation and direction and also depend on the sizes, edges, and shapes of h-BN flake.

Keywords: Molecular Dynamics, Hexagonal Boron Nitride, Interface, Friction

## ÖZ

### **ALTIGENSEL BORON NİTRÜR VE ALTIN YÜZEYLERİNİN NANOTRİBOLOJİK ÖZELLİKLERİNİN TEORİK OLARAK İNCELENMESİ**

Özcan, Gizem  
Yüksek Lisans, Fizik Bölümü  
Tez Yöneticisi: Doç. Dr. Hande Toffoli

Ocak 2020 , 64 sayfa

Nano ölçekte iki boyutlu yapıların sürtünmeye bağlı özellikleri, özellikle son yıllarda önem kazanmıştır ve iyi bilinen kayganlaştırıcıların ara yüzleri arasındaki etkileşimi anlamak için önemli miktarda araştırma yapılmıştır. Endüstriyel gelişmelerde, bu malzemelerin metal yapılar üzerindeki arayüz özellikleri büyük önem taşımaktadır. Bu nedenle, bu tezde, altıgensel BN ve Au (111) arayüzünü moleküler dinamik simülasyonu kullanarak teorik olarak araştırdık. Çünkü bu iki malzemenin yüzeyleri arasındaki simetri benzerlik oranı çalıştığımız modeli oluşturmamıza olanak sağlamaktadır.

Hesaplama sonuçlarında, sürtünme katsayısının uyguladığımız kuvvetle ters orantılı olarak azaldığını ve bunun sıcaklığa bağlı olarak etkilendiği gözlenmiştir. Bu iki numunenin arasında ki nanotribolojik özelliklerinin kaydırma hızının oryantasyonu ve yönüne büyük ölçüde bağlı olduğunu ve ayrıca altıgensel Boron-Nitrür pulunun boyutuna, uç noktalarına ve şekline bağlı olduğunu gözlemledik.

Anahtar Kelimeler: Moleküler Dinamik, Altıgensel Boron Azot, Arayüz, Sürtünme

To my family

## ACKNOWLEDGMENTS

I would like to express my deepest gratitude to my supervisor, Assoc. Prof. Dr. Hande Toffoli for giving me the opportunity to be a member of her team. She has always motivated and supported me through her guidance at every stage of my master's degree. Also, she is the kindest and one of the smartest people I have ever known, and I feel very lucky for being her student.

I would like to thank the Computational Material Science Group members Cem Maden, Gözdenur Toroman, Ümit Doğan Dağlum and Fırat Yalçın for their insightful suggestions and supports about both science and life.

I am very thankful to Gamze Sökmen, Aylin Özle, and Zeynep Oral courage and being perfect friends. They are always there for me when I needed it.

Also, special thanks to my aunt Suzan Aydın and my grandmother Zekiye Aydın for being in my life.

The final and the biggest thanks go to Emre Köse, the most special person in my life, for unconditional love and support.

## TABLE OF CONTENTS

ABSTRACT . . . . .	v
ÖZ . . . . .	vi
ACKNOWLEDGMENTS . . . . .	ix
TABLE OF CONTENTS . . . . .	x
LIST OF TABLES . . . . .	xiii
LIST OF FIGURES . . . . .	xiv
LIST OF ABBREVIATIONS . . . . .	xviii
CHAPTERS	
1 INTRODUCTION . . . . .	1
1.1 History and Development of Lubricity . . . . .	1
1.2 Boron Nitride . . . . .	3
2 MOLECULAR DYNAMICS . . . . .	7
2.1 Introduction . . . . .	7
2.2 Algorithms . . . . .	8
2.2.1 Verlet Algorithm . . . . .	8
2.2.2 Velocity Verlet Algorithm . . . . .	9
2.3 Interatomic Potentials . . . . .	9
2.3.1 Lennard-Jones Potential . . . . .	10

2.3.2	Tersoff Potential . . . . .	12
2.3.3	Embedded Atom Model Potential . . . . .	13
2.4	Thermodynamic Ensembles . . . . .	13
2.4.1	Microcanonical Ensemble . . . . .	13
2.4.2	Canonical Ensemble . . . . .	14
2.5	Thermostats . . . . .	14
2.5.1	Nosé-Hoover Thermostat . . . . .	14
2.5.2	Langevin Thermostat . . . . .	15
2.5.3	Velocity Re-scaling . . . . .	16
2.5.4	Berendsen Thermostat . . . . .	16
2.6	Preliminary Calculations . . . . .	17
2.6.1	Surface Energy of Au(111) . . . . .	17
2.6.2	Adhesion Energy of Au(111)-hBN . . . . .	18
3	NANOTRIBOLOGICAL INVESTIGATION ON PERIODIC HEXAGONAL BORON NITRIDE AND GOLD INTERFACES . . . . .	21
3.1	Benchmark . . . . .	21
3.2	Production Sample . . . . .	28
3.2.1	Thermostat damping time 0.05 fs . . . . .	29
3.2.2	Thermostat damping time 0.005 fs . . . . .	35
4	NON-PERIODIC HEXAGONAL BORON NITRIDE NANOFLEAK ON GOLD SURFACE . . . . .	41
4.1	Hexagonal h-BN Flake . . . . .	41
4.2	Nanoribbons . . . . .	46
4.2.1	Armchair edge . . . . .	47

4.2.2 Zigzag edge . . . . .	50
5 CONCLUSIONS . . . . .	55
REFERENCES . . . . .	57

## LIST OF TABLES

### TABLES

Table 1.1	Comparison of properties of graphene and h-BN . . . . .	6
Table 2.1	Surface energy values of Au(111) . . . . .	19
Table 2.2	Lennard-Jones parameters . . . . .	20
Table 3.1	The benchmark sample's number of atoms in each group . . . . .	22
Table 3.2	Lateral force per h-BN area at each velocity corresponding temperature for benchmark sample . . . . .	25
Table 3.3	The production sample's number of atoms in each group . . . . .	29
Table 3.4	Lateral force per h-BN area at each velocity corresponding temperature for production sample . . . . .	33
Table 3.5	Lateral force per h-BN area at each velocity corresponding temperature for production sample . . . . .	37
Table 4.1	The number of atoms in armchair edge h-BN sample's . . . . .	47
Table 4.2	Lateral force per area on armchair edge h-BN . . . . .	50
Table 4.3	The number of atoms in zigzag edge h-BN sample's . . . . .	50
Table 4.4	Lateral force per area on zigzag edge h-BN . . . . .	52

## LIST OF FIGURES

### FIGURES

Figure 1.1	Atomic Force Microscopy (AFM) . . . . .	2
Figure 1.2	Top (a) and side (b) view of graphene . . . . .	3
Figure 1.3	Hexagonal lattice structure of Boron-Nitride . . . . .	4
Figure 1.4	Hexagonal lattice structure of Boron-Nitride . . . . .	5
Figure 2.1	The graph of Lennard-Jones pairwise potential energy . . . . .	11
Figure 2.2	Demonstration of Au (111) (a) and Au bulk (b) stuctures . . . . .	18
Figure 2.3	Graph of surface energy Au(111) . . . . .	18
Figure 2.4	The total a, the seperated Au(111) b and h-BN c parts of our sample . . . . .	19
Figure 3.1	The simulation of small structure demonstrations at diferent per- spectives. . . . .	21
Figure 3.2	Lateral force per area vs time for 1 m/s at different temperatures (a) and zoomed interval range (b), (c), (d), (e) with using thermostat damping paramater $\tau = 0.05fs$ on Benchmark . . . . .	23
Figure 3.3	Lateral force per area vs time for 0.1 m/s at different tempera- tures (a), and zoomed interval range (b), (c), (d), (e) with using thermo- stat damping paramater $\tau = 0.05fs$ on Benchmark . . . . .	24

Figure 3.4	Lateral force per area vs time for 0.01 m/s at different temperatures (a), and zoomed interval range ( b), (c), (d), (e) with using thermostat damping paramater $\tau = 0.05fs$ on Benchmark . . . . .	25
Figure 3.5	Friction Coefficient vs. load for temperature dependence at different velocities (a), (b), (c) with using thermostat damping paramater $\tau = 0.05fs$ on Benchmark . . . . .	26
Figure 3.6	Friction Coefficient vs. load for velocity dependence at four different temperatures (a), (b), (c), (d) with using thermostat damping paramater $\tau = 0.05fs$ on Benchmark . . . . .	27
Figure 3.7	The simulation of large structure demonstrations at diferent perspectives. . . . .	28
Figure 3.8	Lateral force per area vs time for 1 m/s at different temperatures (a), and zoomed interval range (b), (c), (d), (e) with using thermostat damping paramater $\tau = 0.05fs$ . . . . .	30
Figure 3.9	Lateral force per area vs time for 0.1 m/s at different temperatures (a), and zoomed interval range (b), (c), (d), (e) with using thermostat damping paramater $\tau = 0.05fs$ . . . . .	31
Figure 3.10	Lateral force per area vs time for 0.01 m/s at different temperatures (a), and zoomed interval range (b), (c), (d), (e) with using thermostat damping paramater $\tau = 0.05fs$ . . . . .	32
Figure 3.11	Friction Coefficient vs. load for temperature dependence at different velocities (a), (b), (c) with using thermostat damping paramater $\tau = 0.05fs$ . . . . .	33
Figure 3.12	Friction Coefficient vs. load for velocity dependence at four different temperatures (a), (b), (c), (d) with using thermostat damping paramater $\tau = 0.05fs$ . . . . .	34

Figure 3.13	Lateral force per area vs time for 1 m/s at different temperatures (a), and zoomed interval range (b), (c), (d), (e) with using thermostat damping paramater $\tau = 0.0005fs$ . . . . .	35
Figure 3.14	Lateral force per area for 0.1 m/s at different temperatures (a), and zoomed interval range (b), (c), (d), (e) with using thermostat damping paramater $\tau = 0.0005fs$ . . . . .	36
Figure 3.15	Lateral force per area vs time for 0.01 m/s at different temperatures (a), and zoomed interval range (b), (c), (d), (e) with using thermostat damping paramater $\tau = 0.0005fs$ . . . . .	37
Figure 3.16	Friction Coefficient vs. load for temperature dependence at different velocities (a), (b), (c) with using thermostat damping paramater $\tau = 0.005fs$ . . . . .	38
Figure 3.17	Friction Coefficient vs. load for velocity dependence at four different temperatures (a), (b), (c), (d) with using thermostat damping paramater $\tau = 0.005fs$ . . . . .	38
Figure 4.1	The hexagonal h-BN flake on Au (111) surface simulation at different perspectives . . . . .	41
Figure 4.2	The hexagonal h-BN flake slide on $\hat{x}$ . . . . .	42
Figure 4.3	Friction force of hexagonal h-BN on $\hat{x}$ . . . . .	42
Figure 4.4	The hexagonal h-BN flake slide make a $10^\circ$ angle on $\hat{x}$ . . . . .	43
Figure 4.5	Friction force of hexagonal h-BN on $\hat{x}=10^\circ$ . . . . .	43
Figure 4.6	The hexagonal h-BN flake slide make a $15^\circ$ angle on $\hat{x}$ . . . . .	44
Figure 4.7	Friction force of hexagonal h-BN on $\hat{x}=15^\circ$ . . . . .	44
Figure 4.8	The hexagonal h-BN flake slide make a $20^\circ$ angle on $\hat{x}$ . . . . .	45
Figure 4.9	Friction force of hexagonal h-BN on $\hat{x}=20^\circ$ . . . . .	45

Figure 4.10	Lateral force per area on h-BN for different angled velocity . . .	46
Figure 4.11	The total structures of h-BN nanoribbons with different edges (a), (b) . . . . .	46
Figure 4.12	Armchair edges of h-BN with two different widths (a, b) . . . .	48
Figure 4.13	Armchair edges of h-BN with $v=1$ m/s . . . . .	48
Figure 4.14	Armchair edges of h-BN with $v=0.1$ m/s . . . . .	48
Figure 4.15	Armchair edges of h-BN with $v=0.01$ m/s . . . . .	49
Figure 4.16	Zigzag edges of h-BN with two different widths (a, b) . . . . .	51
Figure 4.17	Zigzag edges of h-BN with $v=1$ m/s . . . . .	51
Figure 4.19	Zigzag edges of h-BN with $v=0.01$ m/s . . . . .	51
Figure 4.18	Zigzag edges of h-BN with $v=0.1$ m/s . . . . .	52

## LIST OF ABBREVIATIONS

### ABBREVIATIONS

MD	Molecular Dynamics
h-BN	hexagonal Boron Nitride
AFM	Atomic Force Microscope
FFM	Friction Force Microscope
LJ	Lennard Jones
EAM	Embedded Atom Model
2D	2 Dimensional
ns	nanosecond
fs	femtosecond
LAMMPS	Large-scale Atomic/Molecular Massively Parallel Simulator

## CHAPTER 1

### INTRODUCTION

#### 1.1 History and Development of Lubricity

Lubricity on flake-like materials was first attributed to Bragg [1], Tomlinson [2] investigated friction at the molecular scale for solid structures, and revealed the energy losses caused by the sliding of contacting solids. Kinetic friction creates an opposite drag force when solid layers are sliding on each other [3]. Friction at the atomic-scale was first interpreted by Hirano [4], which is similar to Tomlinson's solid friction idea, where he investigated friction between two crystal surfaces, which depends on contact surfaces between the crystal surfaces [5]. The idea behind lubricity in nanomaterials continues to be improved and investigated, especially nowadays, both theoretically and experimentally.

Two-dimensional frictional properties in nanomaterials have been investigated in recent years, particularly graphene [6],  $MoS_2$  [7], and h-BN [8] have been identified as low frictional materials. Friction control provides efficiency in energy for the mechanical process and reduces the cost. Also, using a two-dimensional lubricant interface sliding on metal substrates [9] has yielded great results for reducing the friction force since these two-dimensional materials have a weak interaction force between interlayers in the substrate which are useful choices to use as a lubricant [10].

Nanotribological investigations are carried out by using Atomic Force Microscopy (AFM) [11] or Friction Force Microscopy (FFM) [12] for measuring the normal and lateral forces with different modes that are contact, non-contact, and tapping modes. AFM and FFM tips are generally coated by Si [13] and Pt [14]. A simple representation of AFM is given in Figure. 1.1 (adopted from [15]). Frictional behaviors of

2D materials have been studied with AFM [16] [17] [18] and FFM [19] [20] [21], and these 2D lubricants decrease the friction force. Metal substrate surfaces used commonly are Au(111) and Si(111) surfaces [22] [23]. The friction between samples depends on the contact area, the number of atomic layers, the sliding direction, and the tip shape [24].

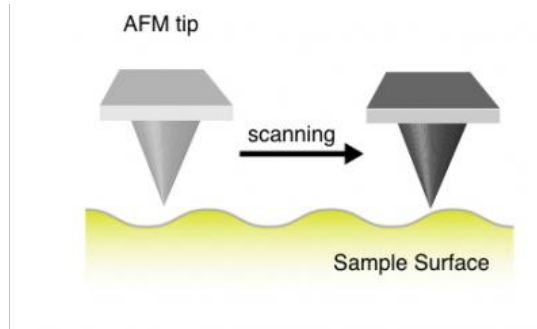


Figure 1.1: Atomic Force Microscopy (AFM)

Theoretical studies on nanotribology have been carried out using computational methods, and there are two main methods, density functional theory (DFT), which is an ab initio method and molecular dynamics. DFT calculations are used to investigate the electronic structure of many-electron systems in an affordable way [25] [26] [27] [28]. Molecular dynamics (MD) is based on Newtonian mechanical calculation. Unlike the DFT, MD consists of a large number of atoms or molecules and mainly used for investigation of the systems' thermodynamic properties. MD has been extensively used for modeling AFM and FFM in different thermodynamic ensembles and different thermostats. These simulations run various loads, velocities, orientations, and directions in different heat baths. Since most experiments are conducted at room temperature, MD simulations give realistic results and helping explain kinetic friction in theoretic computations [29] [30] [31] [32].

Graphene is a 2D honeycomb lattice structure consisting of carbon atoms with  $sp^2$  hybridization, and the lattice structure of the graphene sheet is shown in Figure. 1.2, which material one of the most used 2D material as a lubricant since it is unique mechanical, electronic, optical, and thermal properties. In 2010, the Nobel Prize was given to the experimental isolation of single-layer graphene [33]. Both theoretical

and experimental results proved that graphene reduces the friction and wear between the surfaces [34] [35] [36]. These extraordinary features of graphene contribute to investigate other 2D graphene-like materials such as MoS<sub>2</sub> and hexagonal Boron-Nitride (h-BN). The structural similarities between graphene and h-BN that especially have pointed out tribological studies on h-BN. The properties of this structure will be discussed in the next section in more detail.

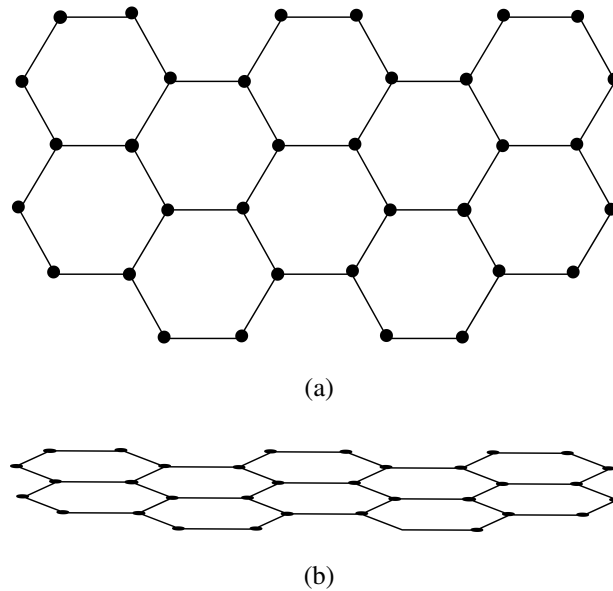


Figure 1.2: Top (a) and side (b) view of graphene

## 1.2 Boron Nitride

Boron Nitride exists in four different arrangements of boron and nitrogen atoms; one of the forms is amorphous (a-BN), and the other three formations are in a crystal structure. These are wurtzite (w-BN), cubic (c-BN), and hexagonal (h-BN). The hexagonal form was first synthesized by Balmain in 1842 [37], but the first stable phase was synthesized in the late 20<sup>th</sup> century. The hexagonal form of B-N is known as graphitic boron nitride, in which the lamellar structure has very similar to graphite. That consists of the same amount of boron and nitride atoms and makes  $sp^2$  hybridization. Structural patterns of h-BN are a form of nanoflake (2D), nanoribbon (1D), nanotube (1D), and fullerene (0D), which illustrated in Figure.1.3 (adopted from [38]),

and these models have different characteristics and stability [39]. It can be used in many fields due to its various properties that are biomedical, technological devices, and aerospace industry [40] [41]. In this section, we mainly have focused on the form of the h-BN structure due to the distinct features of BN.

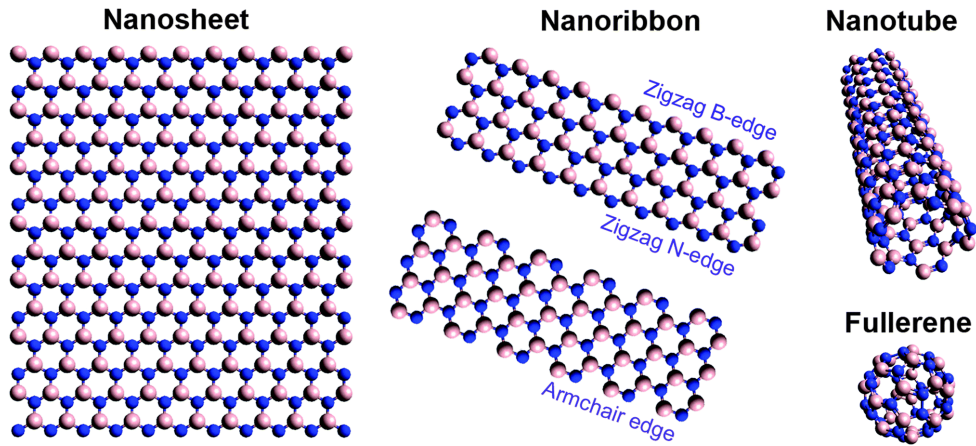


Figure 1.3: Hexagonal lattice structure of Boron-Nitride

The unit vectors of h-BN flake are  $\vec{a}_1$  and  $\vec{a}_2$  and the lattice constant is nearly 1.44 that are shown in Figure. 1.4;

$$\vec{a}_1 = a \begin{pmatrix} \frac{3}{2}, \frac{\sqrt{3}}{2} \end{pmatrix}$$

$$\vec{a}_2 = a \begin{pmatrix} \frac{3}{2}, -\frac{\sqrt{3}}{2} \end{pmatrix}$$

$a$  describes the bond length between the boron and nitrogen atoms. The reciprocal

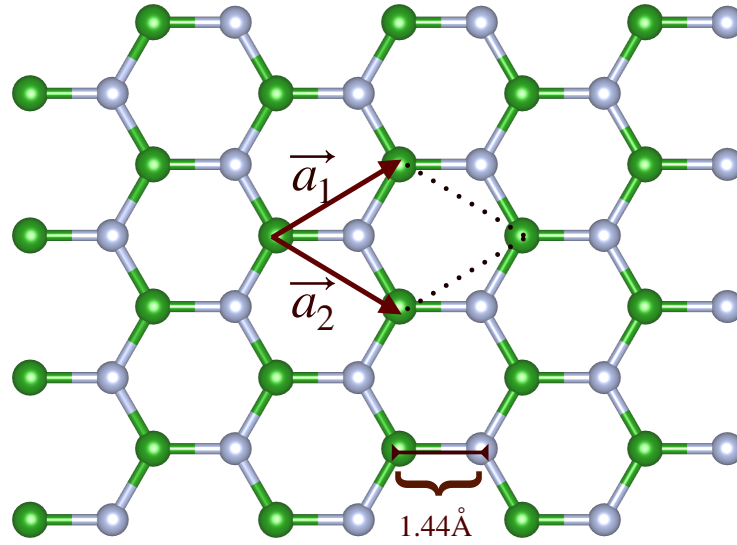


Figure 1.4: Hexagonal lattice structure of Boron-Nitride

unit vectors are given as;

$$\vec{b}_1 = \frac{2\pi}{a} \left( \frac{1}{3}, \frac{\sqrt{3}}{3} \right)$$

$$\vec{b}_2 = \frac{2\pi}{a} \left( \frac{1}{3}, -\frac{\sqrt{3}}{3} \right)$$

The crystallographic structure of h-BN is nearly the same as graphene and with a very similar lattice constant (graphene lattice constant is  $1.42\text{\AA}$ ). Despite this similarity between graphene and BN, there are mechanically different properties. Single layered graphene Young's modulus is nearly 1 TPa ( $\sim 342\text{Nm}^{-1}$ ) when the effective thickness of graphene is 0.335 nm. The breaking strength of the graphene change between 70 and 130 GPa, and it has a zero bandgap at Dirac point. However, the layered graphene structure has a different results strength and elastic modulus of graphene inversely proportional to the thickness of this sample, which can be caused by weak vdW interlayer interaction. Mono layered BN elastic modulus is  $0.865 \pm 0.073$  TPa with 0.334 nm effective thickness. The fracture strength BN nanosheet is between 68 and 215 GPa, and the bandgap is nearly 6 eV. Unlike the graphene, the layered structure of BN has similar results in terms of strength and Young's modulus. Also,

BN is more resistible in high temperatures, since oxidization of graphene starts at  $300^{\circ}C$ , but BN does not oxidize  $800^{\circ}C$  in air. [42] [43] [44]. To compare discussed mechanical properties given in Table. 1.1 to illustrate explicitly ;

Table 1.1: Comparison of properties of graphene and h-BN

Property	Graphene	h-BN
Lattice constant	1.42Å	1.44Å
Bandgap	0 eV	~ 6 eV
Fracture strength	70-130 GPa	68-215 Gpa
Young's modulus	1 TPa	$0.865 \pm 0.073$ TPa
Oxidation resistance	$300^{\circ}C$	$800^{\circ}C$

These distinct mechanical properties of h-BN nanosheets can be used in many different fields in the industry. Due to electrical insulation, high thermal conductivity, low friction, and high-temperature oxidation resistance and chemical stability make it an excellent coating material for metals and ceramics. Also, h-BN is highly sensitive since it has a different surface adsorption energy with different conformations, which is suitable to use in sensing applications [45].

Besides, these features of h-BN also it is an excellent lubricant like other 2D nanomaterials. The anti-wear and anti-frictional properties of BN with high thermal stability and strength draw attention to nanotribology investigations in recent years, both theoretically and experimentally [46].

In this thesis, we investigated the nano tribological properties of the h-BN/Au (111) interface as a molecular dynamics (MD) simulation in different temperatures, shapes, sizes, and edges. The method will be discussed in Chapter 2, and a detailed analysis of our results explained the following chapters.

## CHAPTER 2

### MOLECULAR DYNAMICS

#### 2.1 Introduction

Molecular Dynamics (MD) is a method for computing many-body systems structural properties by means of evaluating their trajectories in time [47]. The interaction between components of a system is modeled by using interatomic potentials, which is the leading factor in determining the accuracy of an MD simulation. The parametrization of these potentials is performed via fitting to data from experimental work or accurate quantum mechanical calculations.

The force on the  $i^{th}$  atom can be obtained from the gradient of the potential where  $\vec{r}_i$  is the position of the  $i^{th}$  atom.

$$\vec{F}_i = -\nabla_i U(\vec{r}_1, \vec{r}_2, \dots, \vec{r}_N) \quad (2.1)$$

From Newton's second law, the force can also be written as;

$$\vec{F}_i = m_i \frac{d^2 \vec{r}_i}{dt^2} \quad (2.2)$$

In MD simulations, Eq.2.2 is integrated numerically in time by means of selecting an appropriate time interval,  $\Delta t$ , and solving for each time step with the help of information from previous steps in an iterative manner. Once a time series of positions is determined, statistical averages can be calculated. There are several integration algorithms that the Verlet algorithm, and Velocity Verlet algorithm are used the most frequently in literature [48]. In the MD calculations presented in this thesis, we use the open-source software LAMMPS (Large-scale Atomic/Molecular Massively Parallel Simulator) [49].

## 2.2 Algorithms

In MD calculations, most of the integration algorithms are based on a Taylor expansion to update velocities and positions of atoms at each time step. Some examples are Verlet, Leap-frog, Velocity Verlet, and Beeman's algorithms [48], [50]. As, general rule algorithms should be fast, efficient, and conserve energy and momentum. The Verlet and velocity Verlet algorithms used in our LAMMPS calculations are discussed in the following subsections.

### 2.2.1 Verlet Algorithm

Loup Verlet developed this algorithm in 1967 [48]. Taylor expansion of particle position at an arbitrary point, around time  $t$  for a small timestep  $dt$  in the forward and backward direction is given by;

$$\vec{r}(t + \Delta t) = \vec{r}(t) + \dot{\vec{r}}\Delta t + \frac{1}{2!}\ddot{\vec{r}}\Delta t^2 + \frac{1}{3!}\dddot{\vec{r}}\Delta t^3 + \mathcal{O}(\Delta t^4) \quad (2.3)$$

$$\vec{r}(t - \Delta t) = \vec{r}(t) - \dot{\vec{r}}\Delta t + \frac{1}{2!}\ddot{\vec{r}}\Delta t^2 - \frac{1}{3!}\dddot{\vec{r}}\Delta t^3 + \mathcal{O}(\Delta t^4) \quad (2.4)$$

Summation of Eq. 2.3 and Eq. 2.4 yields;

$$\vec{r}(t + \Delta t) + \vec{r}(t - \Delta t) = 2\vec{r}(t) + 2\frac{1}{2!}\ddot{\vec{r}}\Delta t^2 \quad (2.5)$$

$$\vec{r}(t + \Delta t) = 2\vec{r}(t) + 2\frac{1}{2!}\ddot{\vec{r}}\Delta t^2 - \vec{r}(t - \Delta t) = 2\vec{r}(t) + \frac{F(t)}{m}\Delta t^2 - \vec{r}(t - \Delta t) \quad (2.6)$$

The new positions of atoms have an error at the order of  $\Delta t^4$ , and the time step in MD is  $\Delta t$ . When the time step decreases, the accuracy of simulation increases. At the same time, the simulation time increases. Choosing the correct  $dt$  for a given simulation is, therefore, finding a balance between accuracy and computational time. In addition to the fact that the velocity of atoms does not calculate this algorithm, velocities depend on other functions like temperature, and that calculation needs extra calculation. To remedy this, a better but equivalent algorithm has been developed.

### 2.2.2 Velocity Verlet Algorithm

The Velocity Verlet Algorithm was first proposed in 1982 [51]. This algorithm's derivation similar to Verlet Algorithms, subtract Eq. 2.3 and Eq. 2.4 each other.

$$\vec{r}(t + \Delta t) - \vec{r}(t - \Delta t) = 2\dot{\vec{r}}\Delta t + \mathcal{O}(\Delta t^3) \quad (2.7)$$

or

$$v(t) = \frac{\vec{r}(t + \Delta t) - \vec{r}(t - \Delta t)}{2\Delta t} + \mathcal{O}(\Delta t^2) \quad (2.8)$$

In this algorithm velocity accurate up to  $\Delta t^{2th}$  order. Also, there are time-invariance for these two algorithms.

### 2.3 Interatomic Potentials

The integration algorithms highlighted above need the evaluation of interatomic forces. Due to the very high cost of treating the interatomic interactions quantum mechanically, empirical potentials are developed that treat the electrons indirectly rather than explicitly. The accuracy of a calculation depends very sensitively on the accuracy of the interatomic potential. In general, the empirical potential function of N-term system is;

$$U(\vec{r}_1, \vec{r}_2, \vec{r}_3, \dots, \vec{r}_N) = \sum_i U_1(\vec{r}_i) + \sum_i \sum_{j>i} U_2(\vec{r}_i, \vec{r}_j) + \sum_i \sum_{j>i} \sum_{k>j} U_3(\vec{r}_i, \vec{r}_j, \vec{r}_k) + \dots \quad (2.9)$$

In Eq. 2.9  $U_1$  is the one body term that corresponds to boundary conditions or external field of system,  $U_2$  is the pair potential (two-body) term which is dependent only spacing between the pair of atoms and the last term  $U_3$  is the three-body potential with the addition of third atom pair interaction is modified. The  $U_3$  and higher orders correspond to many-body potential. The most commonly used interatomic potentials are;

#### Pair potentials

- Lennard-Jones [52], [53]
- Morse [54]

## Many-body potentials for metallic systems

- Embedded Atom Model (EAM) [55] [56]
- Modified EAM (MEAM) [57]
- Finnis and Sinclair (FS) [58]

## Many-body potentials for covalently bounded systems

- Tersoff [59]
- Force-Field Methods (Molecular Mechanics potentials) [60]
- Stillinger-Weber [61]

In the next subsections will briefly discuss Lennard-Jones as a pairwise potential, Tersoff, and EAM for a many-body potential, which is used in our MD calculations.

### 2.3.1 Lennard-Jones Potential

Lennard-Jones [52] [53] potential is one of the most commonly used and simple pair of potential types, that describe potential energy between the two non-bonded atoms or molecules. The Lennard-Jones pair potential graph shown in Figure.2.1 (adopted from [62]).

In this approximation, the potential energy between two atoms as a function of inter-atomic distance is given by the expression.

$$U_{LJ} = 4\epsilon \left[ \left( \frac{\sigma}{r} \right)^{12} - \left( \frac{\sigma}{r} \right)^6 \right] \quad (2.10)$$

In Eq. 2.10 the first term is Pauli-Repulsion, and the second term is van der Waals attraction. There are two important parameters, the  $\sigma$  is a measure of the minimum distance between the two atoms, and  $\epsilon$  is the bond energy between these atoms. These two parameters are taken from UFF (Universal Force Field) [63].

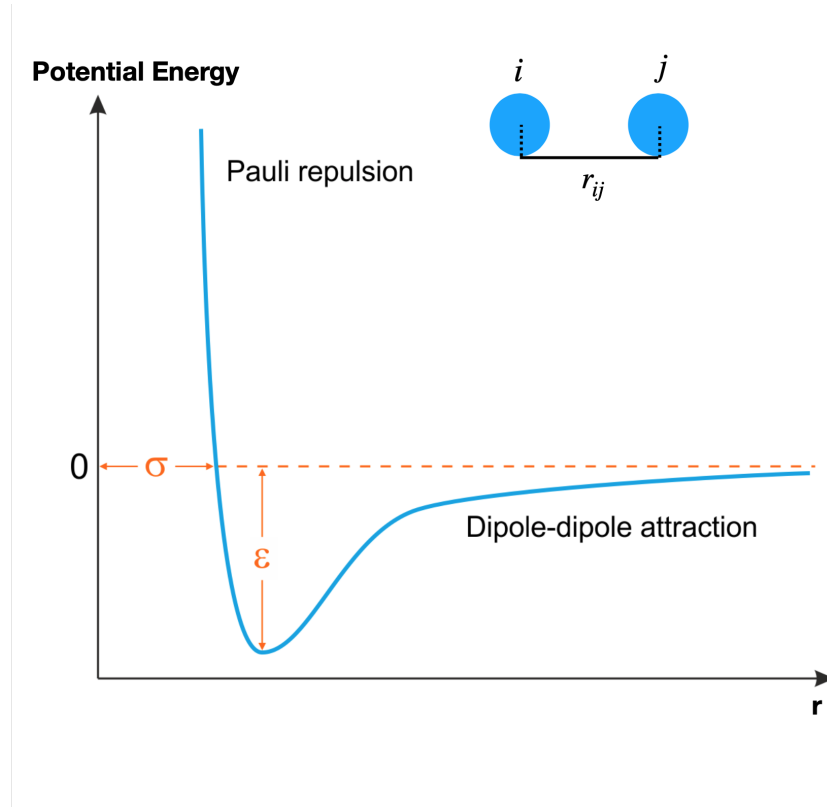


Figure 2.1: The graph of Lennard-Jones pairwise potential energy

In our research, since the sample consist of gold and boron-nitride atoms, these two parameters have to be calculated for interaction between two different kinds of atoms. Therefore, Lorentz-Berthelot combining rule has to be applied to determine the accurate Lennard-Jones parameters.

$$\sigma_{ij} = \frac{\sigma_{ii} + \sigma_{jj}}{2} \quad (2.11)$$

$$\epsilon_{ij} = \sqrt{\epsilon_{ii}\epsilon_{jj}} \quad (2.12)$$

The Lorentz [64] formula given in Eq. 2.11,  $i$ , and  $j$  represents the different atom types shown in Figure.2.1 and the Berthelot [65] formula given in Eq. 2.12. The LAMMPS command for our sample Lennard-Jones potential is given below;

```
## Usage of Lennard-Jones potential in LAMMPS
pair_style hybrid style2 lj/cut cutoff style2
pair_coeff type1 type2 lj/cut $epsilon $sigma cutoff
```

```
pair_coeff type1 type3 lj/cut $epsilon $sigma cutoff
```

The Lennard-Jones potential computes only pairwise interaction that is not enough to calculate many-body interaction in our sample. For this reason, we used Tersoff [66] and EAM [55] [56] potentials, which are shortly discussed in the following subsections, to describe interaction boron-nitride (BN) and gold (Au) atoms between themselves.

### 2.3.2 Tersoff Potential

Bond order Tersoff potential includes three-body interactions based on covalent bonding systems [59]. This potential has an important role in local geometry since bond strength explicitly depends on environmental parameters. Tersoff potential was first developed for Silicon and Carbon atoms then modified for carbon-based systems like boron-nitride (BN) [67]. The potential function is written as;

$$E = \sum_i E_i = \sum_i \sum_{i \neq j} U_{ij} \quad (2.13)$$

$$U_{ij} = f_C(r_{ij})[f_R(r_{ij}) + b_{ij}f_A(r_{ij})] \quad (2.14)$$

The bond energy is given in Eq. 2.14,  $f_R$  term represents the repulsive, and  $f_A$  represents the attractive pair-potentials. The  $f_c$  is the cutoff function is limited to the range of covalent interaction to reduce the computational cost. The important term is  $b_{ij}$  in the Eq. 2.14 since it represents each bonds strength in their local environments and defined by;

$$b_{ij} = (1 + \beta^n \zeta_{ij}^n)^{\frac{-1}{2n}} \quad (2.15)$$

In Eq. 2.15, the  $\zeta_{ij}$  is the effective coordination number, explicit form written as;

$$\zeta_{ij} = \sum_{k \neq i,j} f_C(r_{ik})g(\theta_{ijk})e^{[\lambda_3^3(r_{ij}-r_{ik})^3]} \quad (2.16)$$

The bond angle between atoms computed from  $g(\theta_{ijk})$  term in Eq. 2.16. Moreover, is dependent on the order of atoms. In our study, we use this potential to describe the B-N interaction, and LAMMPS command of this potential is given below;

```

## Usage of Lennard-Jones potential in LAMMPS
pair_style style
pair_coeff * * BNC tersoff B N C

```

### 2.3.3 Embedded Atom Model Potential

The Embedded Atom Model (EAM) potential was proposed by Daw and Baskes [55] [56], and it describes the bonding in metallic clusters. EAM is a semi-empirical and environmentally dependent potential that based on the Density Functional Theory (DFT) method, where the total energy of a collection of atoms is expressed by a functional of own electrostatic density [68]. Then, the energy of the total system can be written as;

$$E_{tot} = \sum_i \left[ F_i(\rho_i) + \frac{1}{2} \sum_{i \neq j} U(r_{ij}) \right] \quad (2.17)$$

In the Eq. 2.17  $U(r_{ij})$  is the pair interaction, and F represents the embedded atom function in terms of electron charge density  $\rho_i$ . In our sample this potential was used to describe the interaction between Au atoms and LAMMPS command for that potential is;

```

## Usage of Lennard-Jones potential in LAMMPS
pair_style style
pair_coeff * * Au_u3.eam

```

## 2.4 Thermodynamic Ensembles

### 2.4.1 Microcanonical Ensemble

In the microcanonical ensemble number of particles (N), volume (V), and total energy (E) was conserved. Once a system in an NVE ensemble reaches thermal equilibrium, independent variables such as T and P should fluctuate around some average values are will fluctuate around instantaneous values [69].

Implementation is easy, but controlling the macroscopic condition is difficult. Also, the instantaneous temperature affects the kinetic energy when the total energy is constant in the NVE ensemble. It might give inaccurate results if the temperature is not at equilibrium. For these reasons, we use a microcanonical ensemble after the simulation reaches the equilibrium state to make sure both temperature and energy still conserving during the simulation. In general, that ensemble does not correspond to experimental conditions, NPT or NVT ensembles are more appropriate for experimental conditions.

### 2.4.2 Canonical Ensemble

In the canonical ensemble number of particles (N), volume (V), and temperature (T) conserved, therefore it is also called an NVT ensemble. When the system reaches equilibrium at a constant temperature in contact with the heat bath, energy fluctuates around the equilibrium [69]. The temperature is defined in terms of the average kinetic energy as follows;

$$T(t) = \frac{1}{k_B N_f} \sum_i m_i v_i^2(t) \quad (2.18)$$

In the Eq. 2.18  $N_f$  represents the number of degrees of freedom and  $k_B$  represents the Boltzmann constant. The temperature is controlled with thermostats in MD simulations. There are several thermostats commonly used and will be discussed in the next section.

## 2.5 Thermostats

### 2.5.1 Nosé-Hoover Thermostat

Nosé-Hoover thermostat formalism was proposed by Nosé [70] then enhanced by Hoover [71]. The thermostat works by introducing additional degrees of freedom in the Lagrangian, which behave like a thermal reservoir to simulate the MD system in the NVT ensemble. Particle coordinate  $r'_i$ , momentum  $p'_i$ , and time  $t'$  defined in a real system and for the fictitious system with the additional degrees of freedom coordinate

$r_i$ , momentum  $p_i$ , and time  $t$ . These two system's relation shown as;

$$r'_i = r_i, \quad p'_i = \frac{p_i}{s}, \quad t' = \int_0^t \frac{dt}{s} \quad (2.19)$$

In the Eq. 2.19  $s$  is the additional degree of freedom and the Lagrangian of the system in terms of fictitious systems variables given as [70];

$$\mathcal{L} = \sum_{i=1} \frac{m_i}{2} s^2 \dot{r}_i^2 + \phi(r) + \frac{Q}{2} \dot{s}^2 - gkT \ln S \quad (2.20)$$

With this Lagrangian, the equation of motions is solved, and the temperature is controlled. In LAMMPS, the Nosé-Hoover is a default thermostat were applied to a group of atoms with specified initial temperature (Tstart), final temperature (Tstop), and thermostat frequency (Tdamp) in the simulation process. Input code for LAMMPS is given below;

```
## Usage of Nosé-Hoover thermostat in LAMMPS
fix ID group-ID style_name keyword value ...
fix 1 all nvt temp 100.0 100.0 0.1
```

## 2.5.2 Langevin Thermostat

Langevin is one of the stochastic NVT thermostats, where the preset velocity distribution function is maintained by applying random and friction forces. Langevin thermostat changes the equation of motion each time step during simulation, that changes momenta. With the addition of these two forces equation of motion become;

$$\vec{F} = \vec{F}_c + \vec{F}_f + \vec{F}_r \quad (2.21)$$

In Eq. 2.21  $\vec{F}_c$  is the conservative force computed with empirical potentials,  $\vec{F}_f$  is the frictional drag term which is proportional to the velocity of particle and  $\vec{F}_r$  is the force by solvent atoms randomly interacted each other at temperature T. The Langevin thermostat applied has additional term when compared to the Nosé-Hoover thermostat code which is defined as seed. Since this thermostat randomly interact with a stochastic heat bath, the seed parameter has to be defined arbitrarily, and LAMMPS input code is given below;

```

## Usage of Langevin thermostat in LAMMPS
fix ID group-ID langevin Tstart Tstop damp seed keyword ...
fix 1 all langevin 100.0 100.0 0.1 699483

```

### 2.5.3 Velocity Re-scaling

This method scale velocity each time step with given relation;

$$\vec{p}_i = \sqrt{\frac{T_0}{T}} \vec{p}_i \quad (2.22)$$

In Eq.2.22  $T_0$  is the desired temperature, and  $T$  is the instantaneous temperature after updated velocities. Velocity re-scaling method temperature fluctuations are not allowed during the simulation, and since scaling frequency is not robust, this technique is not reliable for MD calculations.

### 2.5.4 Berendsen Thermostat

Berendsen thermostat is based on a velocity re-scaling approach and has improved with a new formulation by Berendsen [72]. The main idea is that the system weakly is coupled with a heat bath and has a coupling constant or heat transfer time scale ( $\tau$ ). The temperature rate of change in each time step is given in Eq. 2.23;

$$\frac{dT}{dt} = \frac{1}{\tau}(T_0 - T) \quad (2.23)$$

Also desired temperature calculated with exponential decay of the system;

$$T = T_0 - C e^{-\frac{t}{\tau}} \quad (2.24)$$

These two modifications in Eq.2.23 and Eq.2.23 using to obtain the scaling factor  $\lambda$  with momentum relation  $\vec{p}_i \rightarrow \lambda$  as;

$$\lambda = \left[ 1 + \frac{\Delta t}{\tau} \left( \frac{T_0}{T} - 1 \right) \right]^{\frac{1}{2}} \quad (2.25)$$

This thermostat fixed some problems in the velocity re-scaling approach, especially that allows the temperature fluctuations, which made more close to the real systems.

Usage command in LAMMPS is very similar to the Nosé-Hoover thermostat, initial (Tstart), and desired (Tfinal) temperature has to be specified and thermostat activation frequency (Tdamp) defined as;

```
## Usage of Berendsen thermostat in LAMMPS
fix ID group-ID temp/berendsen Tstart Tstop Tdamp
fix 1 all temp/berendsen 100.0 100.0 0.1
```

In our study, the Berendsen thermostat has been investigated on production and benchmark samples, which has two different damping parameters in the production sample. Also, the edge effect in flake and nanoribbon systems has been studied in that thermostat, which has been discussed detailed in the next chapters.

## 2.6 Preliminary Calculations

### 2.6.1 Surface Energy of Au(111)

Surface energy is the binding energy between the surface atoms and the bulk form of the material since the surface has incomplete bonding, surface energy correlated to the bulk interactions. This energy is calculated from;

$$\sigma = \frac{E_{Surface} - NE_{Bulk}}{A} \quad (2.26)$$

In Eq. 2.26  $N$  is the number of particles in the system,  $E_{Bulk}$  is the single-atom energy of the bulk sample, and  $A$  is the area of the surface. In our calculation, we first generated a six layer Au(111) and Au bulk that contains 300 atoms.

The Au(111) simulation time is 2 ns, first 1 ns we heated to the desired temperature in Berendsen thermostat then, waited for 0.5 ns NVT ensemble and 0.5 ns NVE ensemble to reach the thermal equilibrium. In the calculation process, we only took the last 0.1 ns of NVE ensemble average as  $E_{Surface}$  and inserted in the Eq. 2.26. The results are given in Table. 2.1 and Figure.2.3;

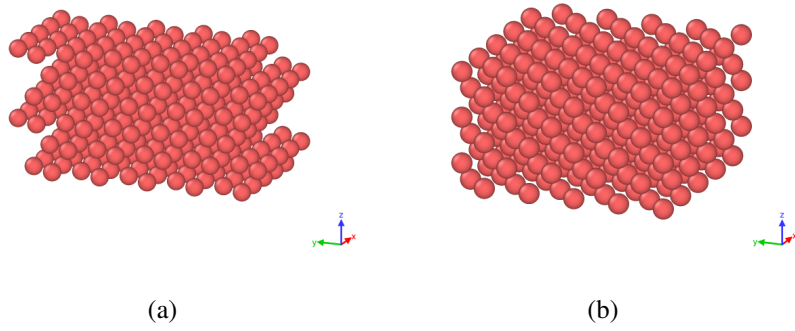


Figure 2.2: Demonstration of Au (111) (a) and Au bulk (b) structures

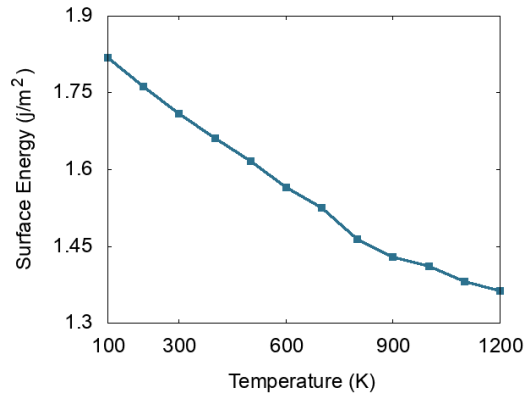


Figure 2.3: Graph of surface energy Au(111)

According to the Table. 2.1 average  $\sigma$  is  $1.5586j/m^2$ , and the experimental result is  $1.51j/m^2$  [73], which is compatible with our results. That shows the Au(111) structure in our MD simulation gives approximately correct outcomes regarding experimental calculations.

### 2.6.2 Adhesion Energy of Au(111)-hBN

Adhesion energy describes the needed energy for the surfaces to cling to each other between the non-identical particles. In our MD calculations, samples were made up of six-layer of Au(111) and a single layer hexagonal BN sheet. Where composed and separated forms of our structure demonstrated in Figure.2.4.

Table 2.1: Surface energy values of Au(111)

Temperature (K)	Energy (J/m <sup>2</sup> )
100	1.8186
200	1.7617
300	1.7091
400	1.6609
500	1.6171
600	1.5645
700	1.5250
800	1.4637
900	1.4286
1000	1.4111
1100	1.3804
1200	1.3629

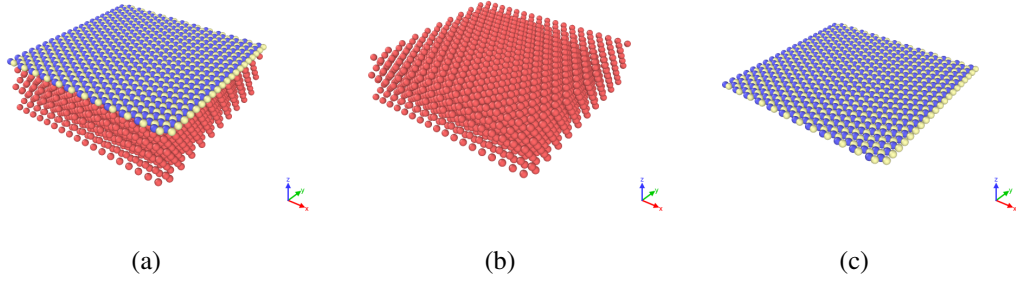


Figure 2.4: The total a, the seperated Au(111) b and h-BN c parts of our sample

This calculation aims to determine correct Lennard-Jones parameters, in our calculation, interatomic potentials, are defined with empirical potentials (Au, BN). On the other hand, there is an interaction between Au and BN, which is long-range interaction, and that defines in LAMMPS with L-J potential, which discussed in pair potential section. These parameters ( $\sigma$ ,  $\epsilon$ ) for nonbonding atoms taken from UFF [63], then using combining rule, obtained results given in Table.2.2.

The adhesion energy of our system was calculated at 1 K using

$$E_{Adhesion} = E_{Total} - E_{Au(111)} - E_{h-BN} \quad (2.27)$$

In Eq. 2.27  $E_{Total}$  is the composed sample ,  $E_{Au(111)}$  seperated Au(111) and  $E_{h-BN}$

Table 2.2: Lennard-Jones parameters

$\sigma_{Au-B}$	3.5085 Å
$\sigma_{Au-N}$	3.2970 Å
$\epsilon_{Au-B}$	0.0036333 eV
$\epsilon_{Au-N}$	0.0022495 eV

seperated hexagonal BN sample energies as;

$$E_{Adhesion} = -15441.484\text{eV} - (-8215.271\text{eV}) - (-7206.4579\text{eV}) \quad (2.28)$$

$$= -19.755\text{eV} \quad (2.29)$$

This results in Eq. 2.28 belongs to the production sample, which has 480 BN units, adhesion energy per BN unit is  $-41.156$  meV. Also, we investigated another sample as a benchmark that is relatively small and strained with respect to the production sample and got  $-40.894$  meV adhesion energy per BN unit. The details of these two samples will be discussed detailed in the next chapter.

## CHAPTER 3

### NANOTRIBOLOGICAL INVESTIGATION ON PERIODIC HEXAGONAL BORON NITRIDE AND GOLD INTERFACES

In this chapter, we present our primary MD investigation on the frictional behavior of two periodic samples simulated in LAMMPS under different conditions using the Berendsen thermostat. A comparison of the results will be discussed.

#### 3.1 Benchmark

The benchmark structure has been used as a test simulation first before running production calculations. Our model consists of the h-BN sheet on top of a Au(111) surface divided into four operational parts.

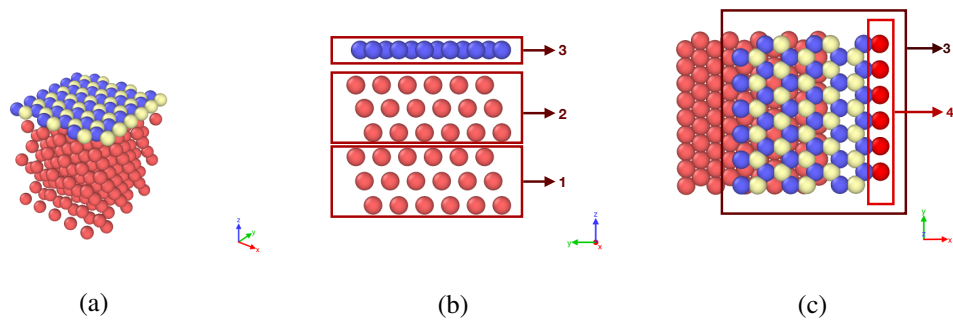


Figure 3.1: The simulation of small structure demonstrations at different perspectives.

This sample consists of six layers of Au along the 111 direction and a h-BN nanosheet, as shown in the Figure.3.1. As seen in Figure.3.1(b), the Au slab is divided into two parts: the lower three layers (labeled 1) is the fixed group, upper three layers (labeled 2) are allowed to move freely during the simulation. The h-BN layer (labeled 3 (c)

has a subgroup (labeled 4), which are driver atoms in the h-BN layer. The driver atoms are a set of atoms that we velocity is only applied to these atoms as opposed to the entire h-BN layer. The number of atoms for every part is given in Table.3.1;

Table 3.1: The benchmark sample’s number of atoms in each group

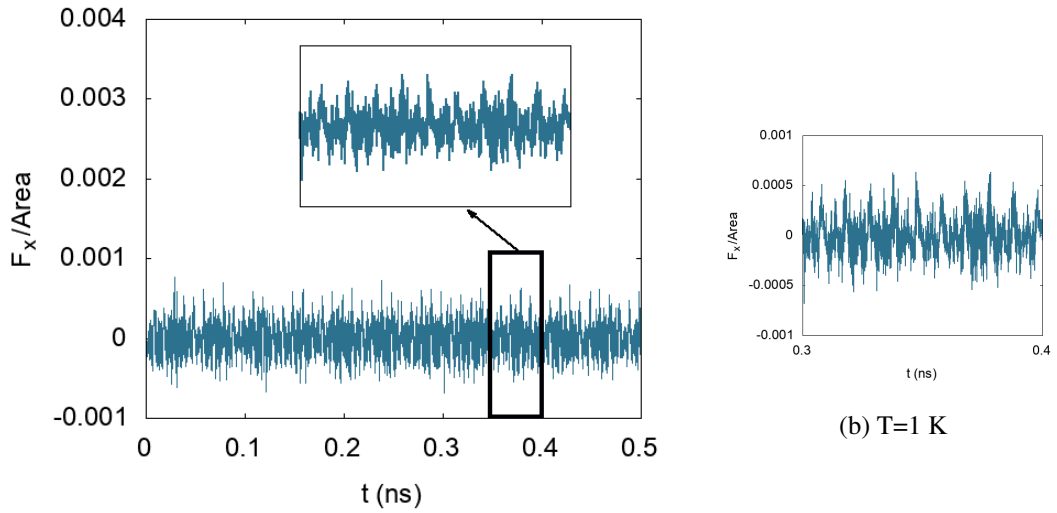
groups	lower part of Au(111)	upper part of Au(111)	h-BN flake	driver atoms in h-BN	Total sample
number of atoms	90	90	72	6	252

These calculations are also useful to understand the axial shear and size effect to compare the previously examined structure. For this small system, a significant lattice mismatch appears. We, therefore, apply a tensile strain of about 11.5 % to the h-BN sheet along the x-direction. Moreover, there are three different interatomic potentials to describe interactions, which are Tersoff for B-N, EAM for Au-Au, and Lennard-Jones between B-N and Au atoms’ that potentials described the Chapter 2 are explained in detail. Once the structure is the MD simulation was performed in a Berendsen thermostat applied only to mobile groups (upper part of Au(111) and h-BN) on the sample. Before examining the frictional properties, the system was heated (2 ns) to the desired temperature then, evolved in NVT (2 ns) and NVE (2 ns) ensembles to reach the thermal equilibrium and thermostat interact with heat bath every 0.05 fs in time step.

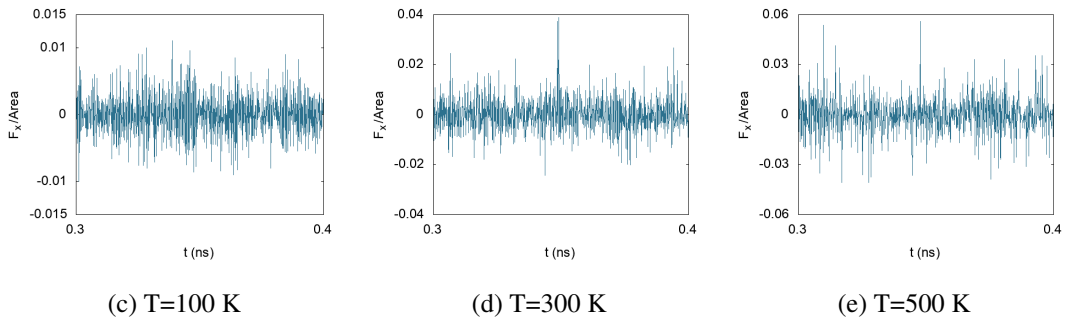
The final and most important part is our MD simulation was the sliding process, as frictional properties of h-BN/Au(111) were investigated in this step. For this purpose, we used different velocities and temperatures when sliding the nanosheet. There are four different temperatures; 1K, 100K, 300K, 500K, and at each temperature, our lubricant moved with velocities of as 1 m/s, 0.1 m/s, and 0.01 m/s along the x-direction. We used simulation times of 0.5 ns for 1 m/s, 5 ns for 0.1 m/s and 50 ns for 0.01 m/s. This allowed a similar distance to be covered at each velocity.

First, we examined the friction force along the x-direction for three velocities and how it changed as a function of temperature. The maximum of the lateral force on the h-BN layer given in Figure.3.2 when moved 1 m/s on the Au(111) surface and the frictional behavior has changed via temperature. In Figure.3.2 (a, b) h-BN made a stick-slip motion at 1 K. On the other hand, at 100 K (c), 300 K (d), and 500 K

(e), become hard to see that motion. The force per area unit has fluctuated nearly between  $\pm 0.0005$  nN/A at 1 K,  $\pm 0.01$  nN/A at 100 K,  $+ 0.04$ , and  $- 0.02$  nN/A at 300 K,  $+ 0.06$  and  $-0.05$  nN/A at 500 K which range increasing proportionally to the temperature.



(a) T=1 K during complete sliding process



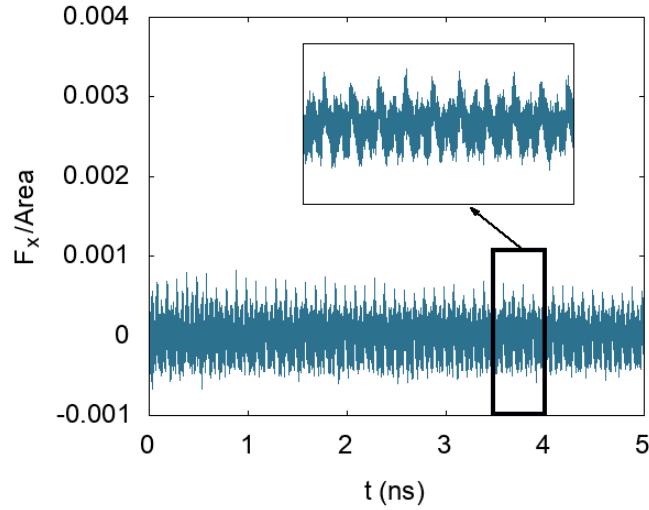
(c) T=100 K

(d) T=300 K

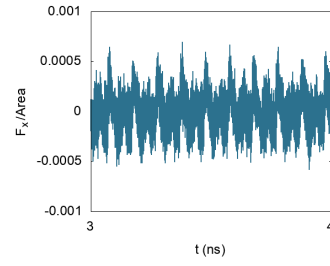
(e) T=500 K

Figure 3.2: Lateral force per area vs time for 1 m/s at different temperatures (a) and zoomed interval range (b), (c), (d), (e) with using thermostat damping parameter  $\tau = 0.05fs$  on Benchmark

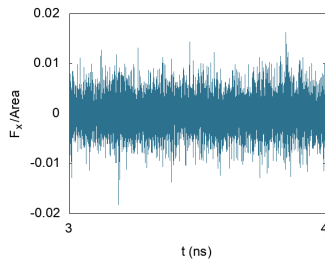
The second velocity (0.1 m/s) yields the result in Figure.3.3 for that calculation. The lateral force changed around  $+ 0.0006$  and  $- 0.0005$  nN/A for 1 K (a, b),  $\pm 0.02$  nN/A for 100 K (c),  $\pm 0.04$  nN/A for 300 K (d) and  $\pm 0.08$  nN/A for 500 K (e). Also, we had similar behavior with  $v=1$  m/s and a slight increase in pressure.



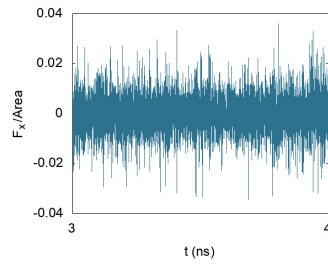
(a) T=1 K during complete sliding process



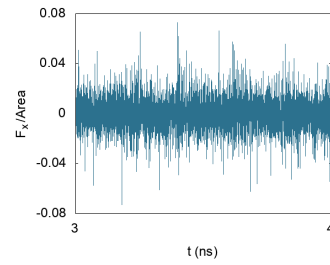
(b) T=1 K



(c) T=100 K



(d) T=300 K

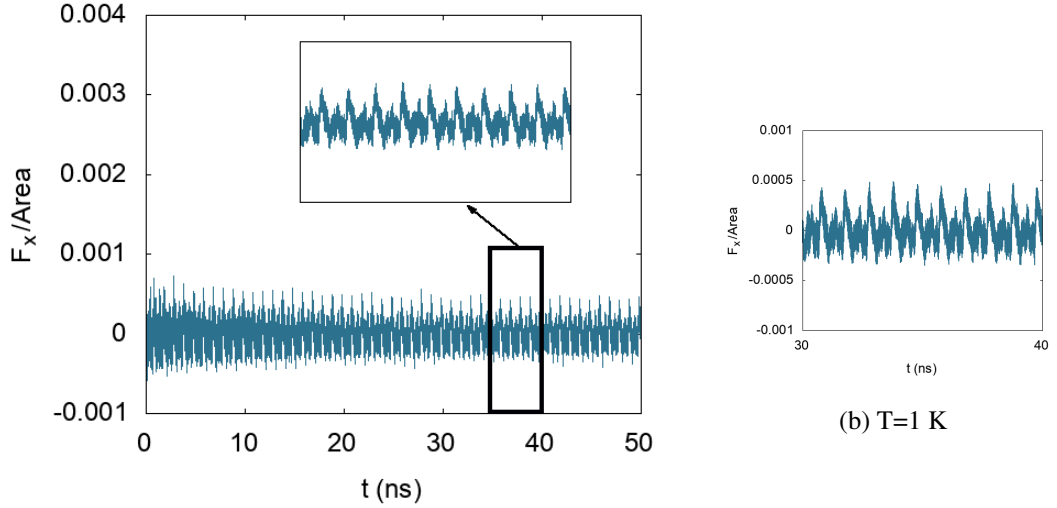


(e) T=500 K

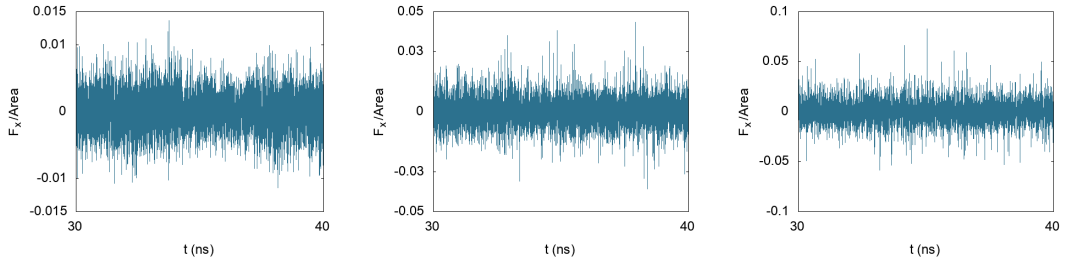
Figure 3.3: Lateral force per area vs time for 0.1 m/s at different temperatures (a), and zoomed interval range (b), (c), (d), (e) with using thermostat damping parameter  $\tau = 0.05 fs$  on Benchmark

Results for the final velocity (0.01 m/s) are given in Figure.3.4 where the lateral force per area fluctuates between + 0.0005 to -0.0004 nN/A at 1 K (b),  $\pm 0.01$  nN/A at 100 K (c), +0.05 to -0.03 nN/A at 300 K (d) and + 0.1 to - 0.05 at 500 K (e).

The lateral force fluctuations per h-BN area for benchmark samples are approximately given in Table.3.2;



(a) T=1 K during complete sliding process



(c) T=100 K

(d) T=300 K

(e) T=500 K

Figure 3.4: Lateral force per area vs time for 0.01 m/s at different temperatures (a), and zoomed interval range ( b), (c), (d), (e) with using thermostat damping parameter  $\tau = 0.05 fs$  on Benchmark

Table 3.2: Lateral force per h-BN area at each velocity corresponding temperature for benchmark sample

velocity	1 K	100 K	300 K	500 K
1 m/s	$\pm 0.0005$ nN/A	$\pm 0.01$ nN/A	- 0.02 to 0.04 nN/A	-0.05 to 0.06 nN/A
0.1 m/s	$\pm 0.0005$ nN/A	$\pm 0.02$ nN/A	$\pm 0.04$ nN/A	$\pm 0.08$ nN/A
0.01 m/s	$\pm 0.0005$ nN/A	$\pm 0.01$ nN/A	- 0.03 to 0.05 nN/A	-0.05 to 0.1 nN/A

We have resembling results and trends for each velocity, temperature highly affected, and increased the force on h-BN nanosheet, and also, the lowering velocity increased

the lateral force but that relatively small to the temperature effect.

So far, the lateral force has been measured in the absence of a vertical load. The next calculation for the benchmark sample is the investigation of friction coefficient with different loads on the h-BN flake and the friction coefficient obtained from;

$$\mu = \frac{f}{N} \quad (3.1)$$

In Eq.3.1  $\mu$  is the friction coefficient,  $N$  is the normal force, and  $f$  is the lateral force in the opposite direction of motion. We consider eleven different loads; 0.25, 0.50, 0.75, 1, 1.25, 1.50, 1.75, 2, 3, 4, and 5 GPa for each temperature and velocity. The friction coefficient has been investigated and compared for different temperatures and velocities.

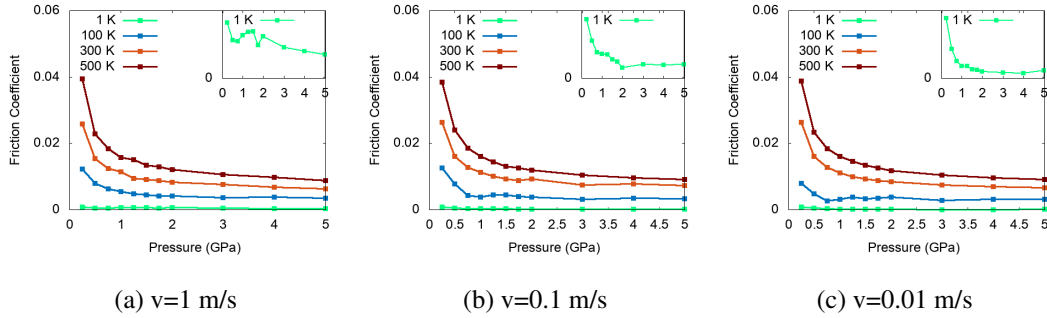


Figure 3.5: Friction Coefficient vs. load for temperature dependence at different velocities (a), (b), (c) with using thermostat damping parameter  $\tau = 0.05fs$  on Benchmark

Friction coefficients for each velocity have obtained, as shown in Figure.3.5. For  $v=1$  m/s, (a),  $\mu$  decays exponentially for all temperatures except 1 K that started with 0.001 and undulated around 0.25 to 2 GPa then decreased linearly to nearly 0.0005 at the highest pressure. When velocity is 0.1 m/s (b) for  $T=500$  K the lateral force has a similar behavior with the previous velocity; however, 300 K and 100 K has a small fluctuations even high pressures and friction coefficient sharply decreased along to 2 GPa and slightly increased at 3 GPa then has been stayed almost same value. For  $v=0.01$  m/s (c), we have observed a similar exponential decreasing for 500 K and 300 K, on the other hand, 100 K friction coefficient results are similar to 0.1 m/s. In

addition, we have a different trend for 1 K at this velocity,  $\mu$  decreased very sharply until 4 GPa, and then it has a slight increment on 5 GPa. In general, the friction coefficient is inversely correlated with the pressure, but the moving speed of h-BN affected these results for low temperatures, especially 1 K, as seen in Figure.3.5.

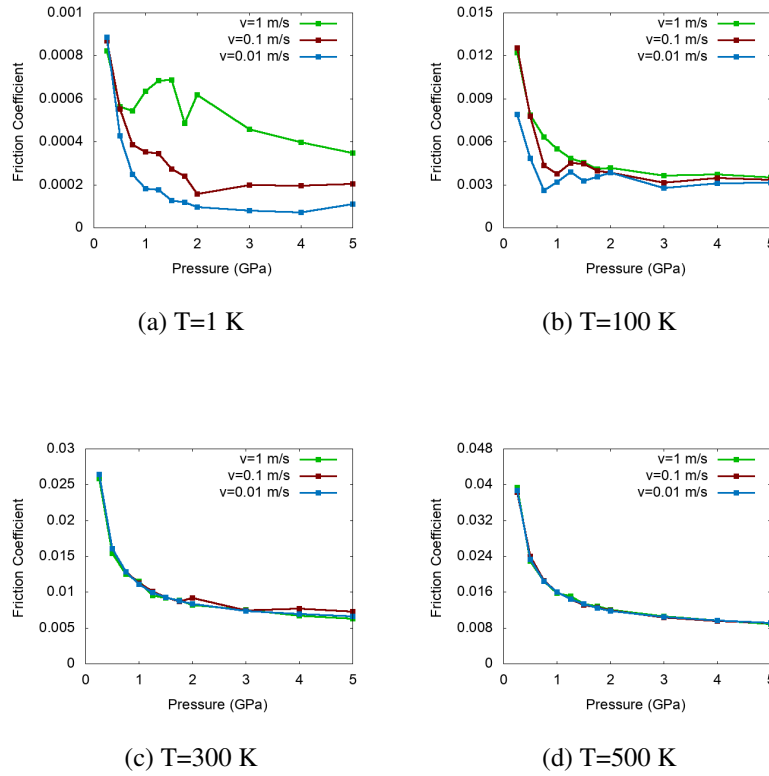


Figure 3.6: Friction Coefficient vs. load for velocity dependence at four different temperatures (a), (b), (c), (d) with using thermostat damping parameter  $\tau = 0.05 fs$  on Benchmark

In Figure.3.6, as shown, the friction coefficient is affected by temperature more than the velocity in applied pressures, and each velocity changed the  $\mu$  differently these temperatures. The lowest temperature 1 K (a)  $\mu$  started around 0.0009 at 0.25 GPa, where the pressure has been effecting the slowest velocity more than others. On the other hand, at 100 K (b) there was opposite situation where the  $\mu$  decreased 0.013 to 0.004 for 1 m/s and 0.008 to 0.004 for 0.01 m/s. When the temperature increased  $\mu$  values become more consistently which chance between 0.027 to 0.006 at 300 K (c) and 0.04 to 0.008 at 500 K (d).

The small size also implies a larger strain, which indirectly allows us to consider the effect of strain on friction behavior. In a smaller sample, we explored more calculation parameters due to the size of this sample. On the other hand, the benchmark sample was not displayed realistic conditions; for this reason, we repeat our calculations in the larger sample as a production sample.

### 3.2 Production Sample

The MD simulation of the h-BN/Au(111) interface investigated as formed using a large number of atoms in this section, and the purpose of this large structure is to be close to real-life experimental observation. Our sample consists of the h-BN sheet on top of a Au(111) surface divided into four operational parts.

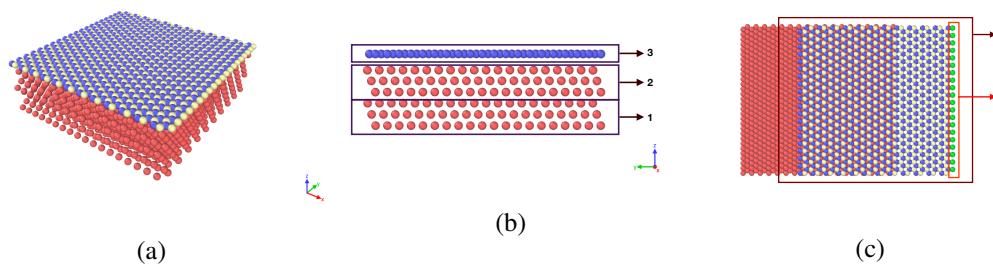


Figure 3.7: The simulation of large structure demonstrations at different perspectives.

This sample consists of six layers of Au along the 111 direction and a h-BN nanosheet, as shown in Figure.3.7. As seen in Figure.3.7(b), the Au slab is divided into two parts: divided two-part; the lower three layers (labeled 1) is the fixed group, upper three layers (labeled 2) are allowed to move freely during the simulation. The h-BN layer (labeled 3) in (c) has a subgroup (labeled 4), that are driver atoms in the h-BN layer. The driver atoms are a set of atoms which we velocity is only applied to these atoms as opposed to the entire h-BN layer. The number of atoms for every part is given in Table.3.3;

When creating the sample, the h-BN layer has been strained by around 0.01 % to fit on Au(111) surface. The general simulation protocol is the same as the benchmark samples; the potentials and thermodynamic ensembles that we used in our MD simu-

Table 3.3: The production sample's number of atoms in each group

groups	lower part of Au(111)	upper part of Au(111)	h-BN	driver atoms in h-BN	Total sample
number of atoms	1080	1080	960	20	3120

lation and also the same thermostat were applied to the same groups of the production sample. First, the system temperature is increased to final temperature (5 ns), after that kept in NVT (5 ns), and NVE (2.5 ns) ensemble while thermally equilibrated with in each  $\tau = 0.05$  fs before moved the h-BN on Au(111) surface.

Then, the frictional behavior of the h-BN/Au(111) interface was examined in this step, which is the main focused part of our study. The sliding velocities are along the horizontal direction where temperatures are at 1 K, 100 K, 300 K and 500 K. This step's simulation length different for each  $v$  that are 1.25 ns for 1 m/s, 12.5 ns for 0.1 m/s and 125 ns for 0.01 m/s.

The production sample examination was repeated at two different thermostat frequencies to see the effect of the heat bath parameters.

### 3.2.1 Thermostat damping time 0.05 fs

In this subsection, we investigated the production sample where the thermostat is applied at every 0.05 fs with a heat bath during the complete sliding process.

First, we examined the friction force along the x-direction for three velocities and how it changed as a function of temperature.

The maximum of the lateral force on the h-BN layer with temperature at velocity 1 m/s as seen in Figure. 3.8. While the stick-slip motion is apparent for the 1K simulation, for higher temperatures, it disappears.

In Figure.3.9, and Figure.3.10, our lateral force results are displayed, as a function of the temperature at a velocity of 0.1 m/s and 0.01 m/s, respectively. Similar observations can be made for these two velocities concerning the stick-slip motion and increasing lateral force with increasing temperature.

Interestingly, when compared across different velocities, our lateral force results come out to be similar for the 0.01 m/s and 1 m/s while the middle velocity, 0.1 m/s, comes out to be different. Further analysis is required to understand the detailed reason behind this behavior.

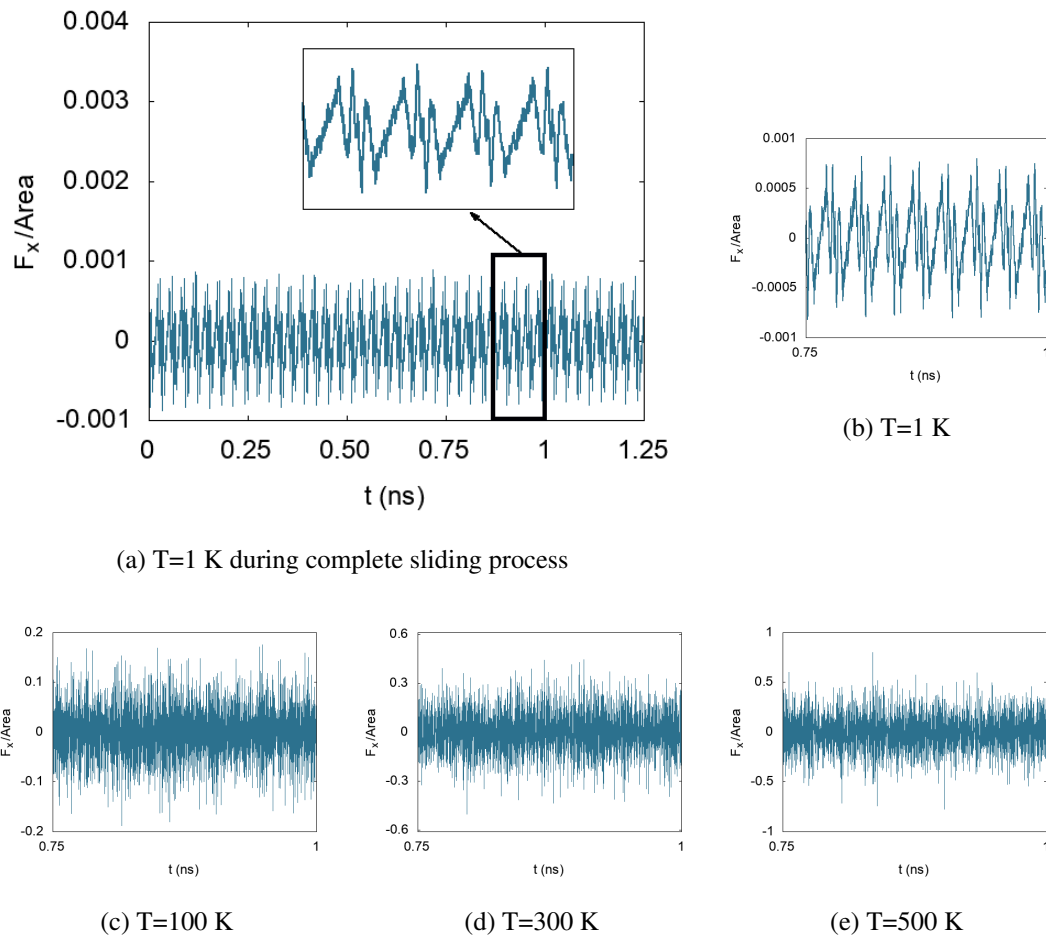
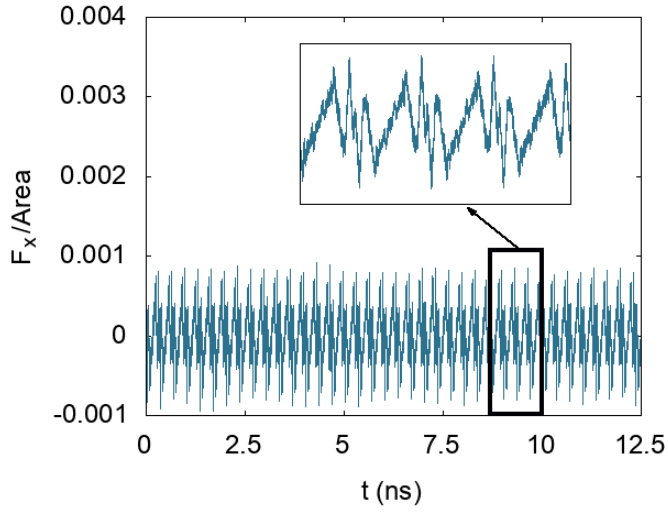
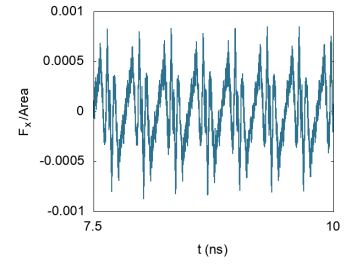


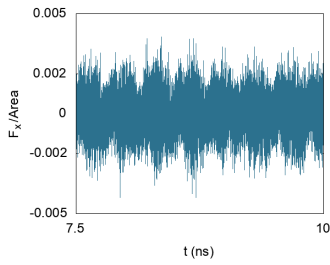
Figure 3.8: Lateral force per area vs time for 1 m/s at different temperatures (a), and zoomed interval range (b), (c), (d), (e) with using thermostat damping parameter  $\tau = 0.05 fs$



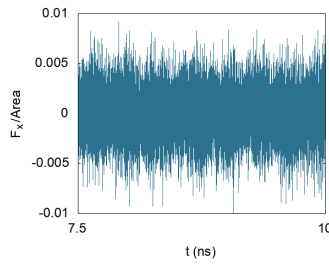
(a) T=1 K during complete sliding process



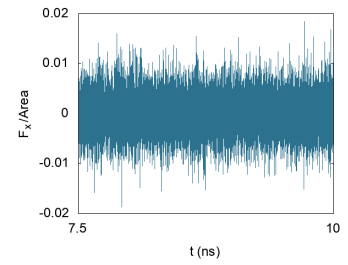
(b) T=1 K



(c) T=100 K

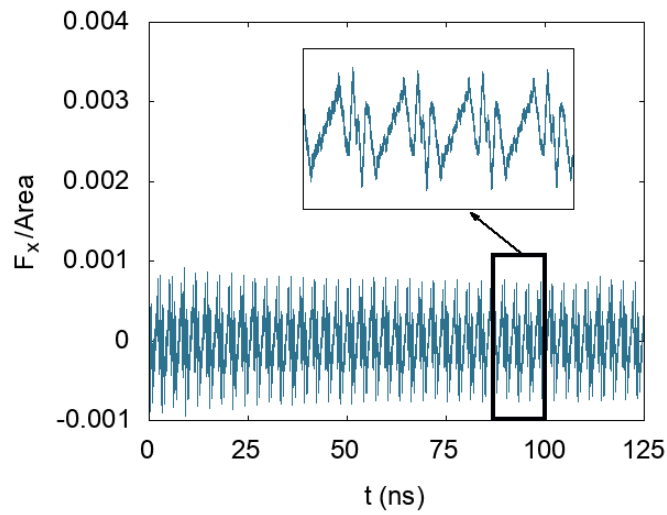


(d) T=300 K

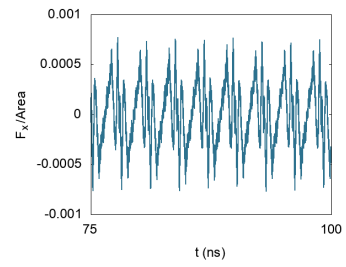


(e) T=500 K

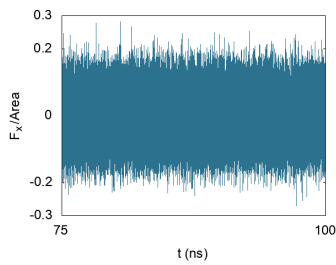
Figure 3.9: Lateral force per area vs time for 0.1 m/s at different temperatures (a), and zoomed interval range (b), (c), (d), (e) with using thermostat damping parameter  $\tau = 0.05 fs$



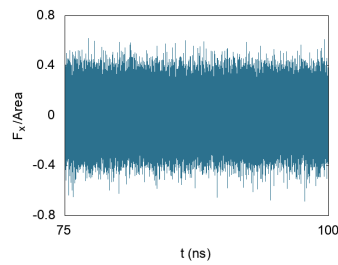
(a) T=1 K during complete sliding process



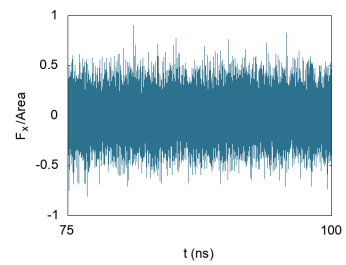
(b) T=1 K



(c) T=100 K



(d) T=300 K



(e) T=500 K

Figure 3.10: Lateral force per area vs time for 0.01 m/s at different temperatures (a), and zoomed interval range (b), (c), (d), (e) with using thermostat damping parameter  $\tau = 0.05 fs$

The lateral force fluctuations for the production sample at  $\tau=0.05$  is approximately given in Table.3.4;

Table 3.4: Lateral force per h-BN area at each velocity corresponding temperature for production sample

velocity	1 K	100 K	300 K	500 K
1 m/s	$\pm 0.001$ nN/A	$\pm 0.1$ nN/A	$\pm 0.3$ nN/A	$\pm 0.5$ nN/A
0.1 m/s	$\pm 0.001$ nN/A	$\pm 0.002$ nN/A	$\pm 0.005$ nN/A	$\pm 0.01$ nN/A
0.01 m/s	$\pm 0.001$ nN/A	$\pm 0.2$ nN/A	$\pm 0.4$ nN/A	$\pm 0.5$ nN/A

The next calculation for the production sample is the investigation of friction coefficient with different loads on the h-BN flake five different loads; 1 GPa, 2 GPa, 3 GPa, 4 GPa, and 5 GPa for each temperature and velocity.

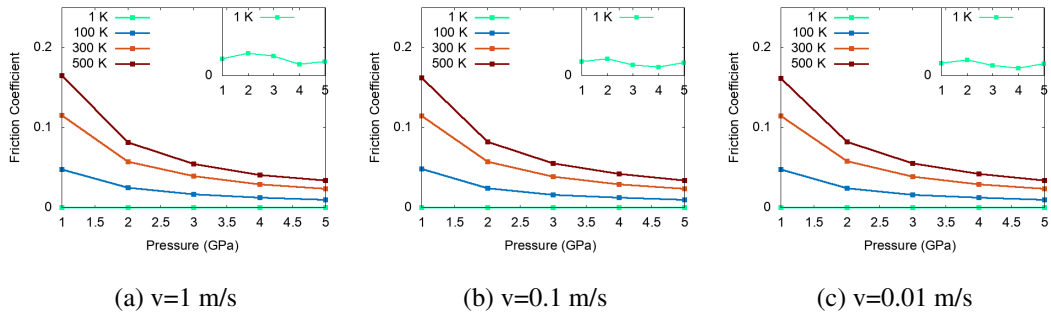


Figure 3.11: Friction Coefficient vs. load for temperature dependence at different velocities (a), (b), (c) with using thermostat damping parameter  $\tau = 0.05 f_s$

First, we analyze the temperature dependence results displayed in Figure.3.11. For all velocities and temperatures investigated, the friction coefficient is seen to decrease as a function of increasing load. This is rather typical behavior for many interfaces involving two-dimensional materials [74]. In addition, we observe a very sensitive dependence on temperature, where for all velocities considered, the friction coefficient steadily increases as a function of temperature. At 500 K  $\mu$  reaches nearly 0.17 for 1 GPa load and sharply decreased to about half this value at 2 GPa. Then the decrease rate becomes smaller with further increasing load. This situation is also valid for 300 K and 100 K, where around the highest load (5 GPa ) friction coefficients

converge to similar values at temperatures for all velocities. 1 K's behavior is rather different from others, where the friction coefficient is nearly zero. We zoom into the 1 K results in each graph in the inset for clarity. The behavior for 1 K is similar for all velocities.

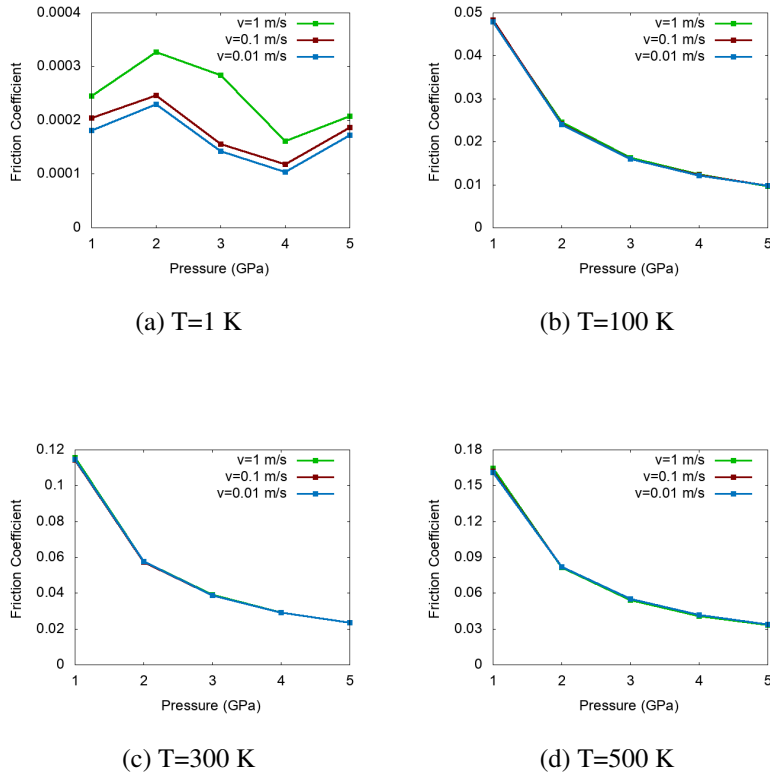
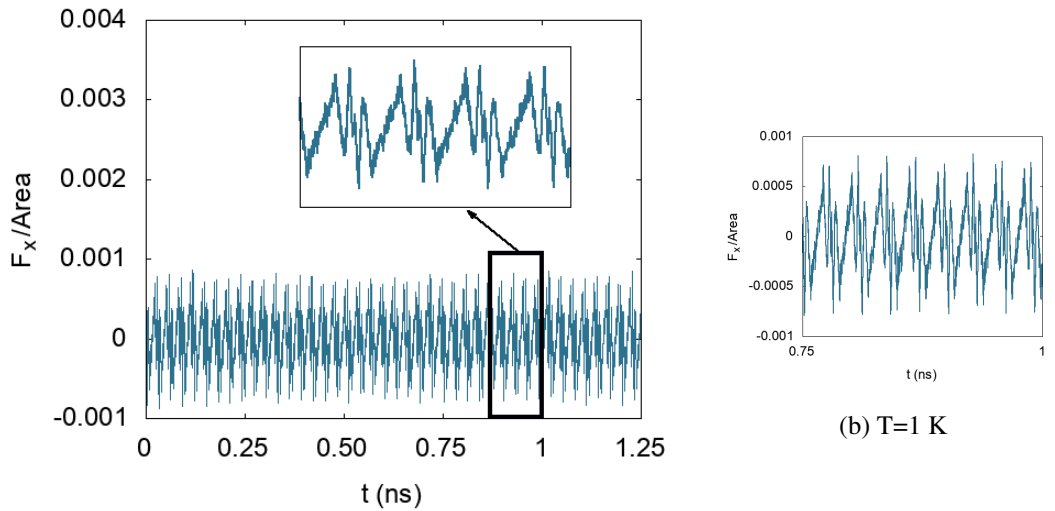


Figure 3.12: Friction Coefficient vs. load for velocity dependence at four different temperatures (a), (b), (c), (d) with using thermostat damping parameter  $\tau = 0.05fs$

In Figure. 3.12 temperature effect is shown more clearly, at 1 K (a), there is a similarity between 0.1 and 0.01 m/s, but the fastest velocity displays relatively higher  $\mu$  than others although the load 5 GPa still has lower  $\mu$  than 1 GPa load.  $\mu$  decreases 0.05 to 0.01 at 100 K (b), 0.12 to 0.02 at 300 K (c) and 0.16 to 0.03 at 500 K (d) for three velocities. In general, the friction coefficient becomes smaller and closer value with higher loads. However, there is very little variation in the friction coefficient as a function of velocity. The difference is seen more apparent for 1 K due to the smaller scale.

### 3.2.2 Thermostat damping time 0.005 fs

In order to eliminate any possible dependencies on arbitrary parameters of the calculation, we repeat the calculations with a different thermostat time, i.e.,  $\tau = 0.005 fs$  in the sliding part, and other variables have been kept the same for each calculation. This allows us to see what happens when the system interacts with the heat bath more rapidly.



(a) T=1 K during complete sliding process

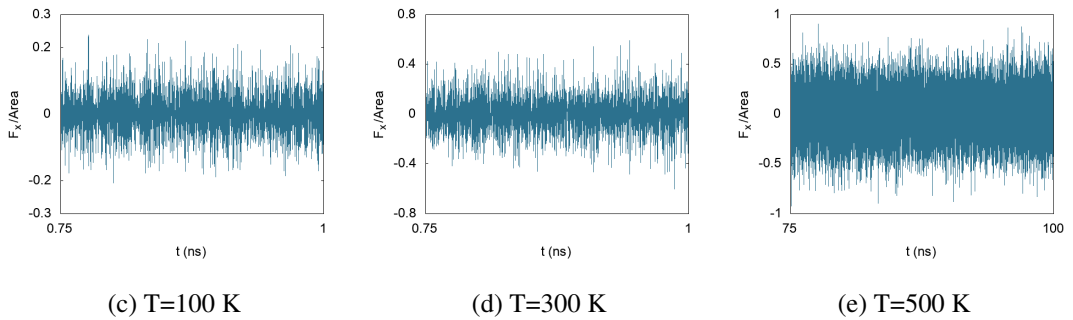
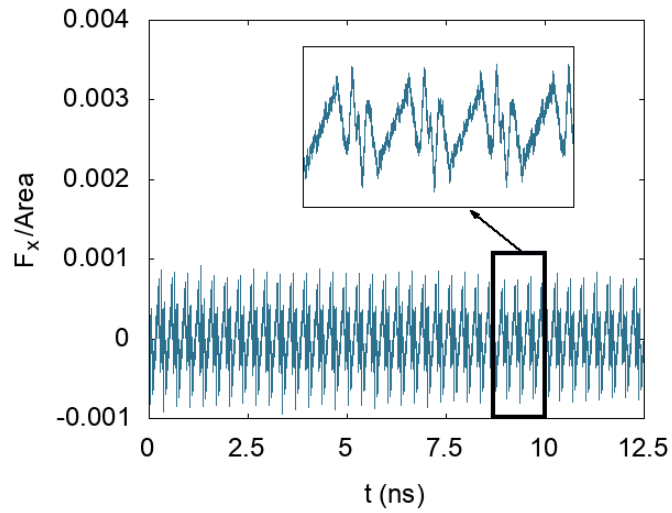
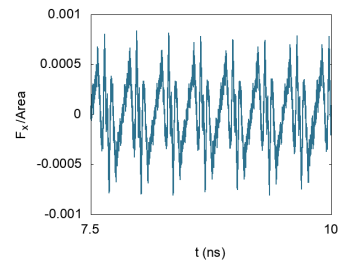


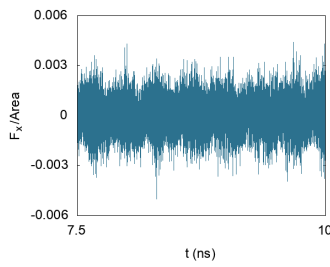
Figure 3.13: Lateral force per area vs time for 1 m/s at different temperatures (a), and zoomed interval range (b), (c), (d), (e) with using thermostat damping parameter  $\tau = 0.0005 fs$



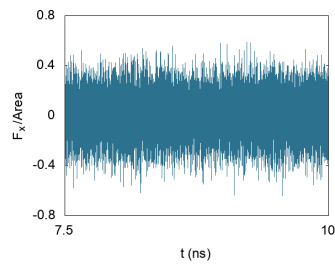
(a) T=1 K during complete sliding process



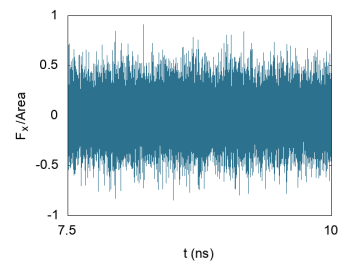
(b) T=1 K



(c) T=100 K

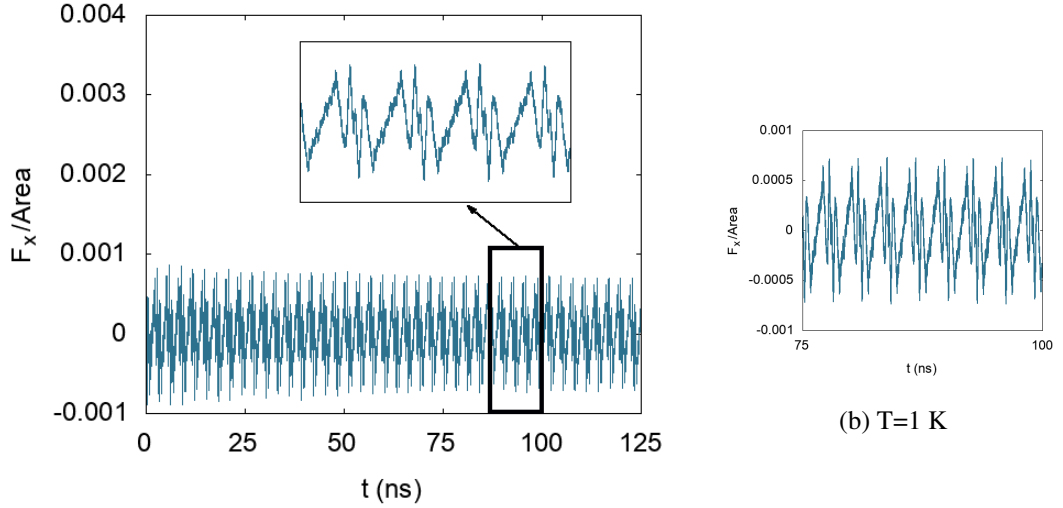


(d) T=300 K



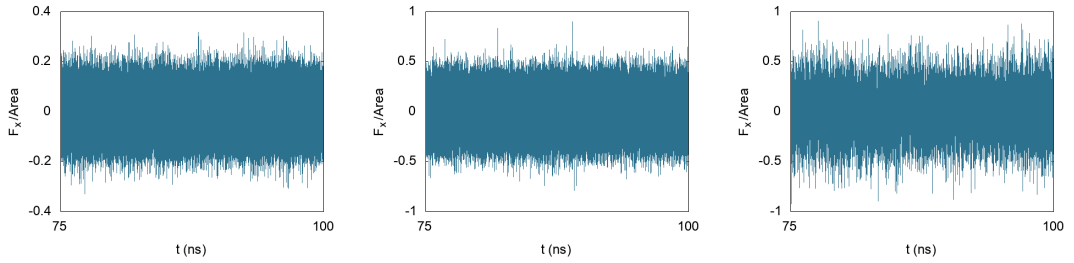
(e) T=500 K

Figure 3.14: Lateral force per area for 0.1 m/s at different temperatures (a), and zoomed interval range (b), (c), (d), (e) with using thermostat damping parameter  $\tau = 0.0005 fs$



(a) T=1 K during complete sliding process

(b) T=1 K



(c) T=100 K

(d) T=300 K

(e) T=500 K

Figure 3.15: Lateral force per area vs time for 0.01 m/s at different temperatures (a), and zoomed interval range (b), (c), (d), (e) with using thermostat damping parameter  $\tau = 0.0005 fs$

The lateral force fluctuations for the production sample at  $\tau=0.005$  are approximately given in Table.3.5;

Table 3.5: Lateral force per h-BN area at each velocity corresponding temperature for production sample

velocity	1 K	100 K	300 K	500 K
1 m/s	$\pm 0.001$ nN/A	$\pm 0.2$ nN/A	$\pm 0.4$ nN/A	$\pm 0.65$ nN/A
0.1 m/s	$\pm 0.001$ nN/A	$\pm 0.003$ nN/A	$\pm 0.4$ nN/A	$\pm 0.55$ nN/A
0.01 m/s	$\pm 0.001$ nN/A	$\pm 0.2$ nN/A	$\pm 0.5$ nN/A	$\pm 0.6$ nN/A

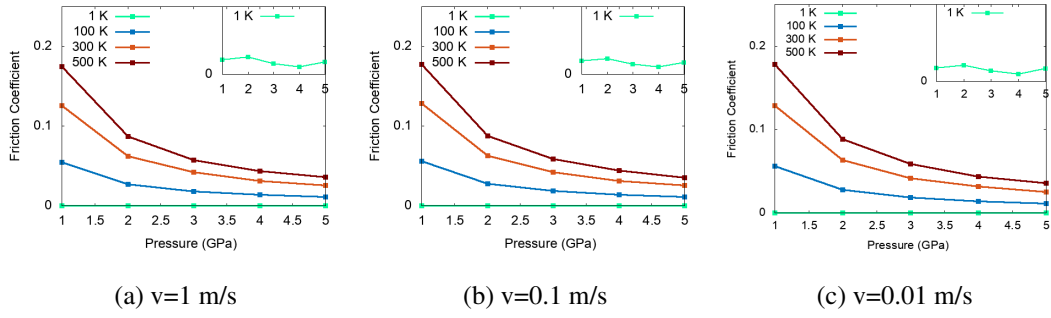


Figure 3.16: Friction Coefficient vs. load for temperature dependence at different velocities (a), (b), (c) with using thermostat damping parameter  $\tau = 0.005 f_s$

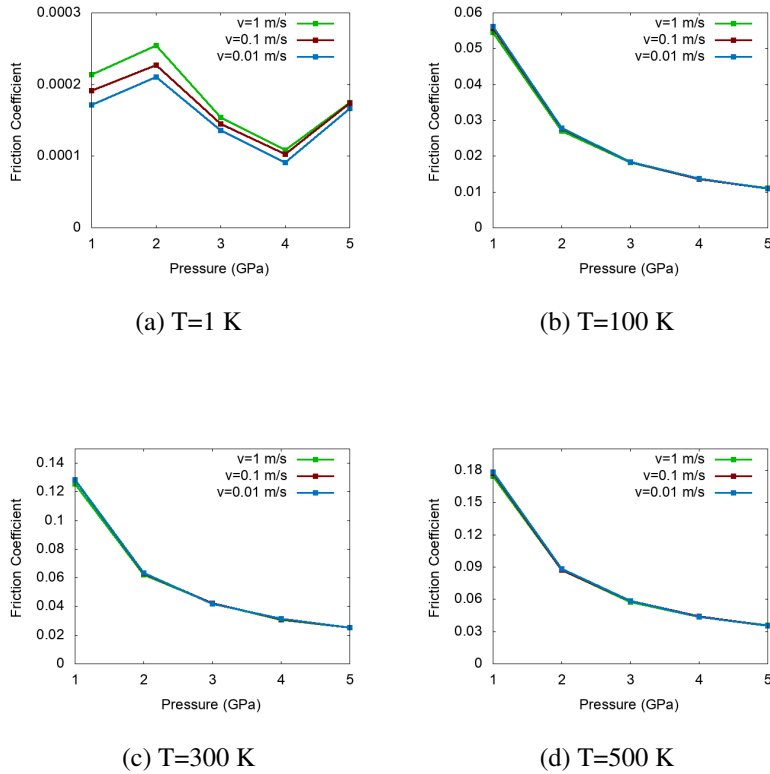


Figure 3.17: Friction Coefficient vs. load for velocity dependence at four different temperatures (a), (b), (c), (d) with using thermostat damping parameter  $\tau = 0.005 f_s$

This subsection proves that the friction coefficient is mostly independent of the thermostat frequency, with only a slight increase for the smaller  $\tau$ . In this section, we have been investigated the production sample's frictional behavior in different envi-

ronments in the Berendsen thermostat with two different thermostat frequencies.

Lubricant properties of h-BN on Au (111) surface has similar trends generally for both of our periodic sample, however large one has given more consistent and higher friction coefficient results as seen in Figure.3.12 that differences might be caused by axial strain on a small sample.



## CHAPTER 4

### NON-PERIODIC HEXAGONAL BORON NITRIDE NANOFLEAK ON GOLD SURFACE

In this chapter, non-periodic h-BN based systems are examined at room temperature, namely hexagonal-shaped h-BN flakes and h-BN nanoribbons of the armchair and zigzag termination on periodic Au(111) surfaces. These calculations aimed to understand shape, size, and edge effects on h-BN tribological behavior as a lubricant.

#### 4.1 Hexagonal h-BN Flake

The hexagonal h-BN flake and Au(111) interfaces are studied for non-periodic h-BN flakes at different shapes and sizes to understand how frictional properties are affected.

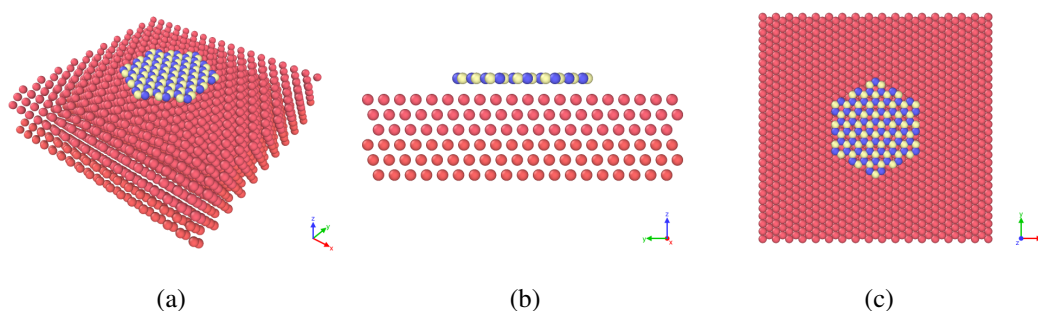


Figure 4.1: The hexagonal h-BN flake on Au (111) surface simulation at different perspectives

The Au(111) part of the structure is still periodic and the same as the production

sample in Chapter3 in terms of groups and number of atoms. However, the h-BN component consists of 114 atoms, and only 6 of them are the driver atoms where velocity was applied. The model is shown in Figure.4.1.

In these MD simulations hexagonal h-BN flake was displaced over Au(111) surface at four different angles which are made  $0^\circ$ ,  $10^\circ$ ,  $15^\circ$  and  $20^\circ$  angles on x-axis to investigate the effects of different registries between the Au(111) and h-BN at 300 K. The simulation protocol is the same with the production sample in Chapter3, where pre-sliding step took 12.5 ns where the total MD simulation lasted 15.5 ns ( $v = 1$  m/s), 42.5 ns ( $v = 0.1$  m/s) and 312.5 ns ( $v = 0.01$  m/s), respectively.

A snapshot from our calculation where the flake is displaced along the x-direction can be seen in Figure.4.2.

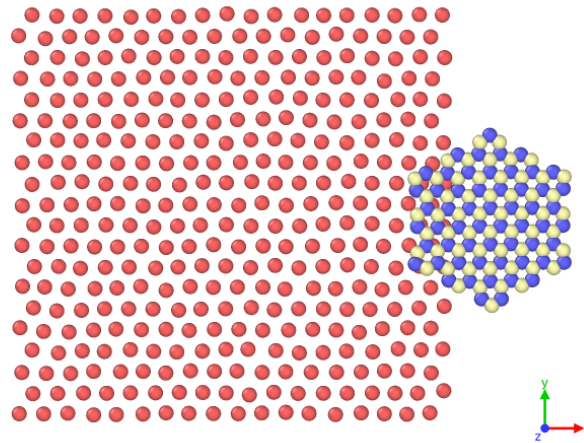


Figure 4.2: The hexagonal h-BN flake slide on  $\hat{x}$

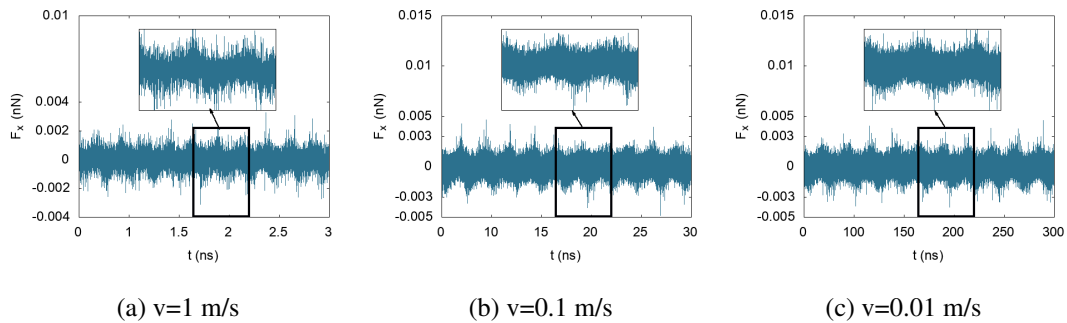


Figure 4.3: Friction force of hexagonal h-BN on  $\hat{x}$

In Figure.4.3 the total lateral, friction force on the flake is examined at three different velocities; interestingly, stick-slip motion is observed at all velocities at 300 K, which is not seen in the production sample at that temperature. The  $F_x$  fluctuated around  $\pm 0.002$  nN at 1 m/s,  $\pm 0.003$  nN at 0.1 m/s, and  $\pm 0.003$  nN at 0.01 m/s when the flake was moving slower.

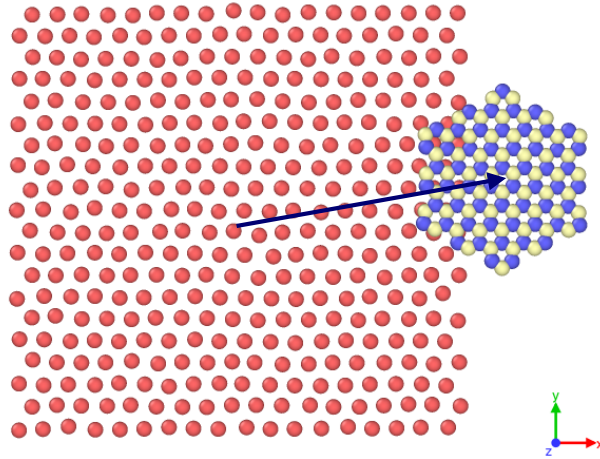


Figure 4.4: The hexagonal h-BN flake slide make a  $10^\circ$  angle on  $\hat{x}$

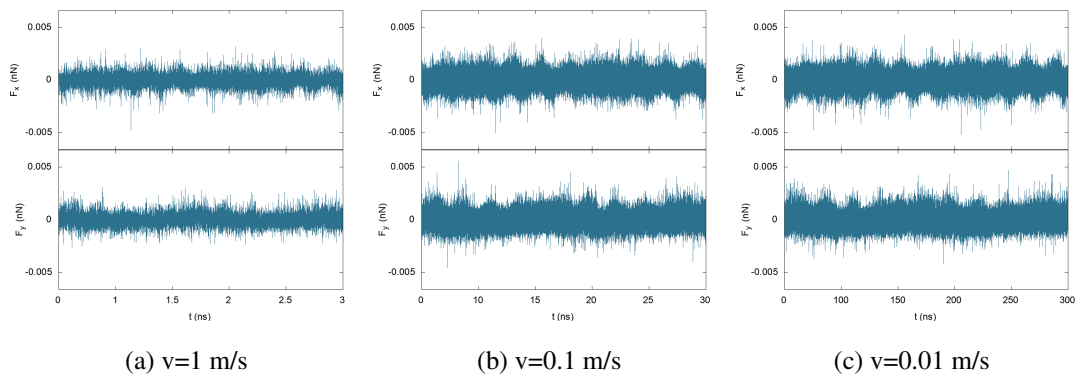


Figure 4.5: Friction force of hexagonal h-BN on  $\hat{x}=10^\circ$

The results obtained for a displacement angle of  $10^\circ$  can be seen in Figure.4.4. These results show that friction force decrease, and the periodic motion was seen rarely, especially at  $v=1$  m/s in Figure.4.5 (a). However, we have similar trends on  $F_x$  since we observed this motion at some points with slower velocities, and an increase in  $F_x$  was observed. Also, we have friction forces on  $\hat{y}$ , which are relatively small to  $F_x$  and not seem to symmetric in their averages.

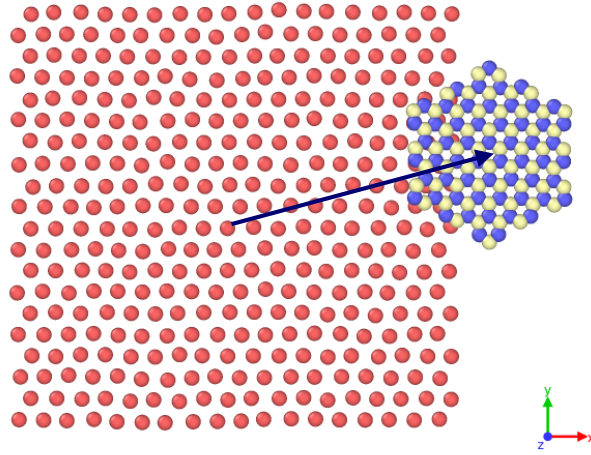


Figure 4.6: The hexagonal h-BN flake slide make a  $15^\circ$  angle on  $\hat{x}$

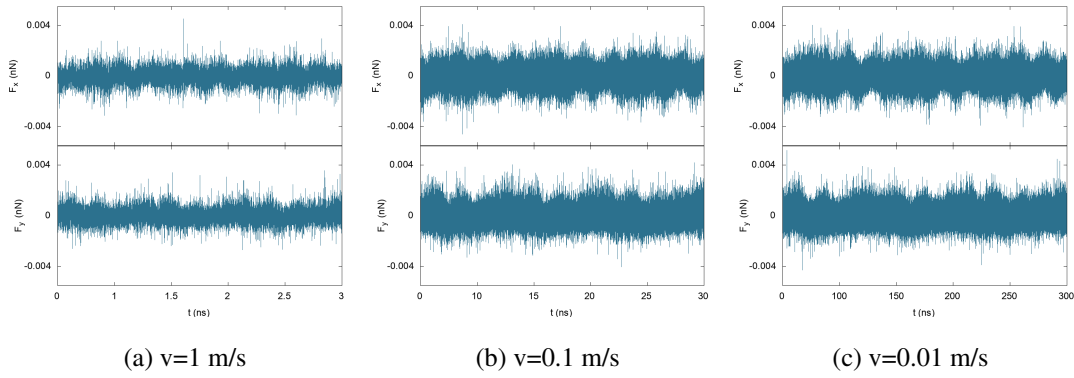


Figure 4.7: Friction force of hexagonal h-BN on  $\hat{x}=15^\circ$

When the angle was increased to  $15^\circ$  (Figure.4.6), we have similar results with the previous study. Furthermore, in this angle, the highest and lowest values of friction force are smaller than  $10^\circ$ , but the average of the range is higher in  $15^\circ$ , and  $F_y$  increased overall since  $v_y$  is getting larger. Although the stick-slip motions occur, they are not seen as clearly as smaller angled velocity.

The last examination on the hexagonal h-BN flake was conducted by pulling the flake at an angle of  $20^\circ$ .  $F_x$  continues to decrease with angle while  $F_y$  grows as the  $v_y$  compound increased. Also, we obtained some trends about this flake's frictional behavior when angle had increased stick-slip motions on  $F_x$  was disappearing, and on  $F_y$ , we observed this motion in positive values.

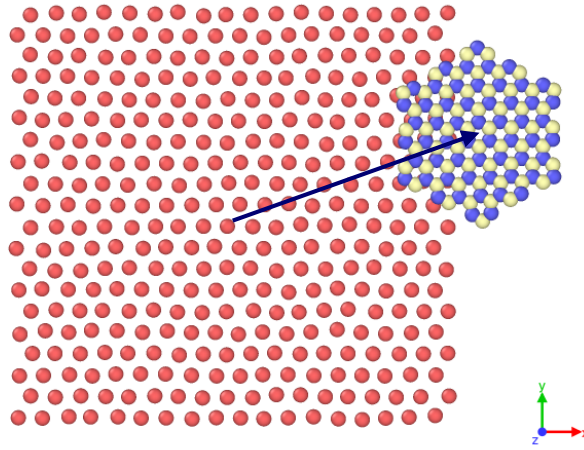


Figure 4.8: The hexagonal h-BN flake slide make a  $20^\circ$  angle on  $\hat{x}$

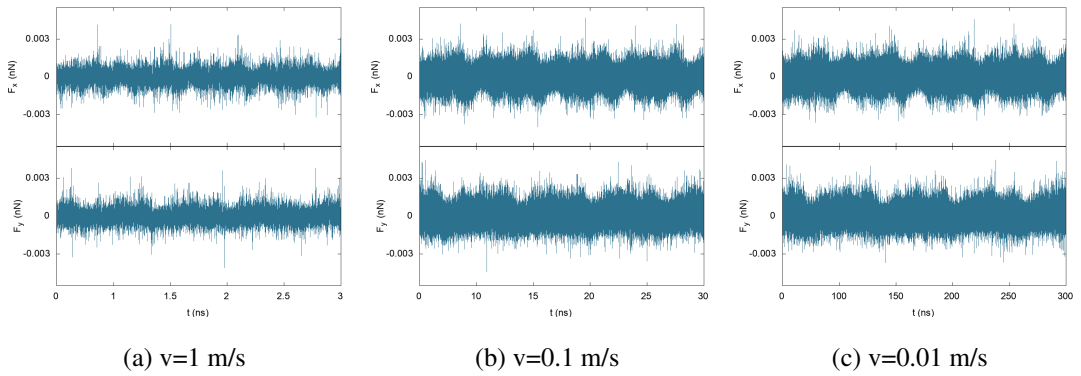


Figure 4.9: Friction force of hexagonal h-BN on  $\hat{x}=20^\circ$

Then we calculated the lateral force; the number of atoms in h-BN flake times average normal forces divided by h-BN area.

In Figure.4.10, lateral friction force per area of h-BN highly dependent on the pulling angle rather than velocity with increased angle. While this increase occurs at a slower rate going from 0 degrees to 10 and then 15, there is a sudden large gap between 15 and 20 degrees. The lateral force increased in the per h-BN area.

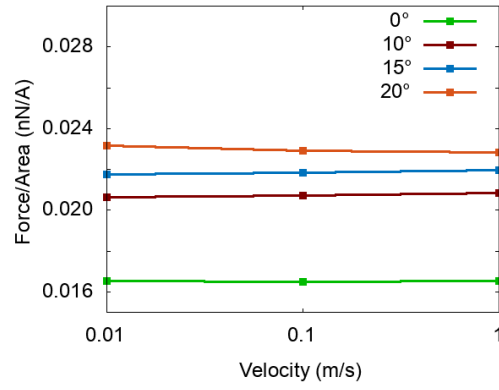
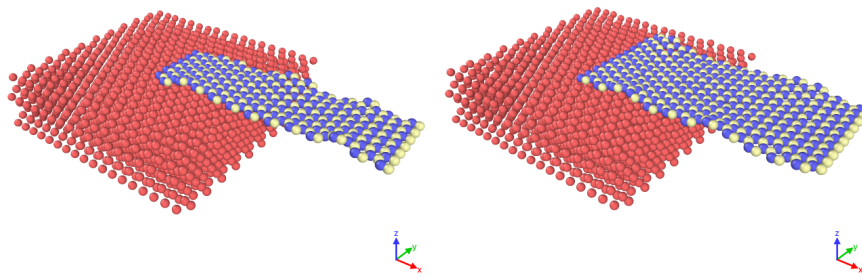
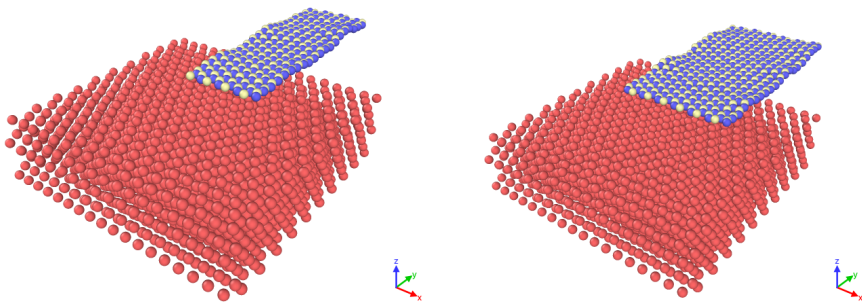


Figure 4.10: Lateral force per area on h-BN for different angled velocity

## 4.2 Nanoribbons



(a) Armchair edges of h-BN



(b) Zigzag edges of h-BN

Figure 4.11: The total structures of h-BN nanoribbons with different edges (a), (b)

In this section, we investigated the edge effects on the tribologic behavior of h-BN using nanoribbons with different widths. h-BN nanoribbons present two different edges

that are armchair and zigzag. We construct the two different edges by means of simply removing some of the atoms while allowing periodicity along the x-direction for the armchair edge and y-direction for the zigzag edge. Also, the simulation process was the same as the hexagonal h-BN flake that valid for our MD simulation time. We made this examination for two different widths on the armchair and zigzag edges, which are shown in Figure.4.11.

#### 4.2.1 Armchair edge

In this subsection, we investigate the frictional properties of an armchair nanoribbon as it slides along the x-axis on the Au(111) surface at 300 K with three different velocities. Our MD simulation contains the same number of Au atom with a production sample, but the number of atoms in the h-BN group was different, which was given in Table.4.1;

Table 4.1: The number of atoms in armchair edge h-BN sample's

groups	h-BN	driver atoms in h-BN
number of atoms for width=14.97 Å	312	7
number of atoms for width=23.69 Å	480	10

In order to isolate the edge effects, we investigate two widths for the same orientation of the nanoribbon. These samples, together with the topmost layer of the substrate, can be seen in Figure.4.12 for the sake of clarity.

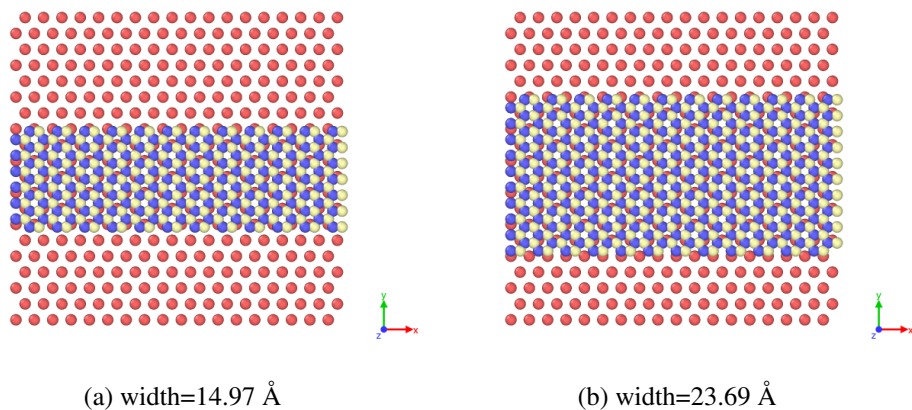


Figure 4.12: Armchair edges of h-BN with two different widths (a, b)

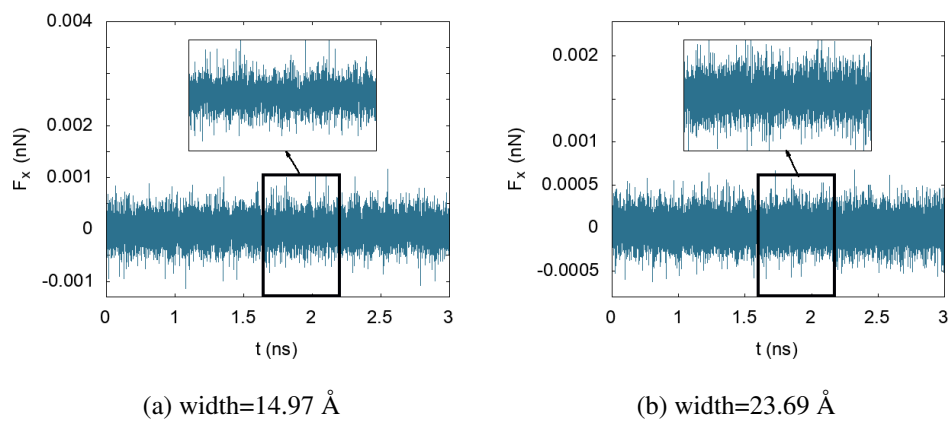


Figure 4.13: Armchair edges of h-BN with  $v=1$  m/s

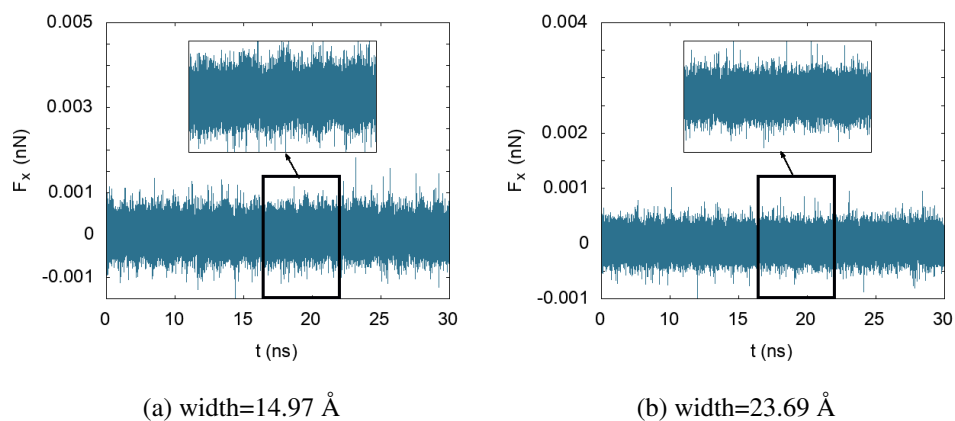


Figure 4.14: Armchair edges of h-BN with  $v=0.1$  m/s

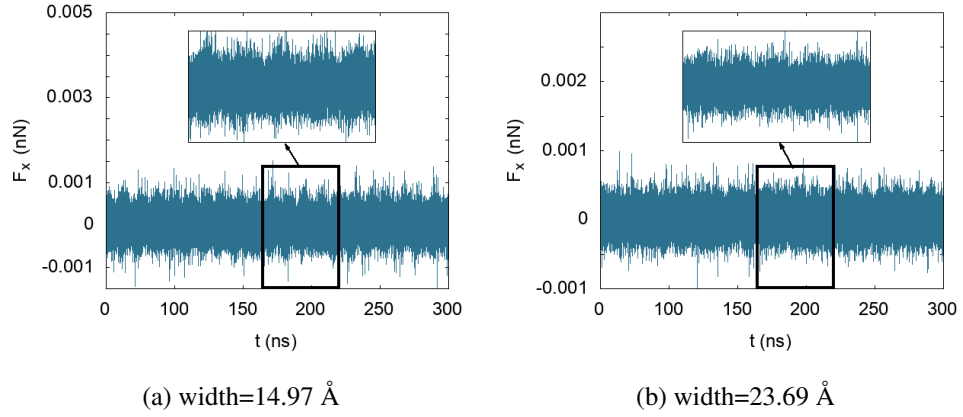


Figure 4.15: Armchair edges of h-BN with  $v=0.01$  m/s

We investigated tribologic properties per atom at our usual three velocities. For  $v=1$  m/s shown in Figure.4.13, the narrower sample experiences a lateral friction force, which fluctuates between nearly  $\pm 0.001$  Nn and the wider sample between  $\pm 0.0005$  Nn. At this velocity, we do not observe stick-slip motion in either structure. For velocity of 0.1 m/s,  $F_x$  was slightly increased, as seen in Figure.4.14 for both widths. For our final velocity of 0.01 m/sec, we observe similar behavior in terms of the magnitude of the friction for each sample to the 0.1 m/sec, as shown in Figure.4.15.

As predicted, the effect of the edges is clearly seen in these results. The larger width appears to experience a lateral friction force, which is about half of that of the smaller width. At the same time, both widths experience friction forces that are smaller than the typical forces experienced by the fully periodic continuous h-BN sheet covered in Chapter.3 . We attribute the striking difference between the behaviors of the two widths to the ratio of the edge atoms to the bulk atoms and also to the coincidence of the Au atoms with the atoms of the h-BN nanoribbons while they slide. The wider ribbon, not only has a smaller edge-to-bulk ratio but also has only one edge that slides directly above a chain of Au atoms in perfect coincidence, as opposed to the narrow ribbon, which has two perfectly coincident edges.

Table 4.2: Lateral force per area on armchair edge h-BN

width of sample	v=1 m/s	v=0.1 m/s	v=0.01 m/s
14.97 Å	0.0061 nN/Å	0.0062 nN/Å	0.0062 nN/Å
23.69 Å	0.0041 nN/Å	0.0041 nN/Å	0.0041 nN/Å

The average friction force on armchair h-BN nanoribbon per area is given in Table.4.2 where the narrower h-BN structure has more considerable friction than the larger one. On the other hand, the effect of the velocity is much more subtle, yielding average friction forces that are largely independent of velocity. This result occurs in spite of the fact that the time-dependent behavior is slightly different for different samples.

#### 4.2.2 Zigzag edge

Our last MD investigation of this chapter is zigzag edged h-BN nanoribbons at 300 K once again using a similar protocol to previous calculations. The sliding direction, however, is along the y-axis, perpendicular to the long side of our substrate. The MD simulation in two different widths and the number of atoms in each h-BN groups given in Table.4.3;

Table 4.3: The number of atoms in zigzagged h-BN sample's

groups	h-BN	driver atoms in h-BN
number of atoms for width=15.84 Å	320	8
number of atoms for width=26.64 Å	520	13

Once again, we investigated the two different widths for both, as seen in Figure.4.16.

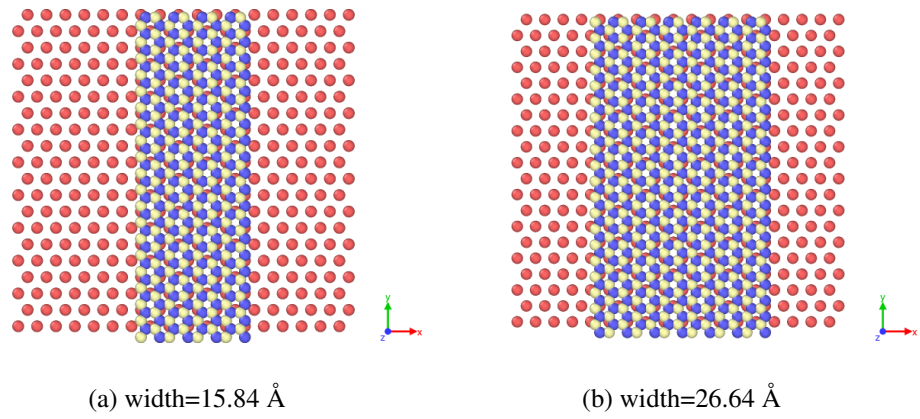


Figure 4.16: Zigzag edges of h-BN with two different widths (a, b)

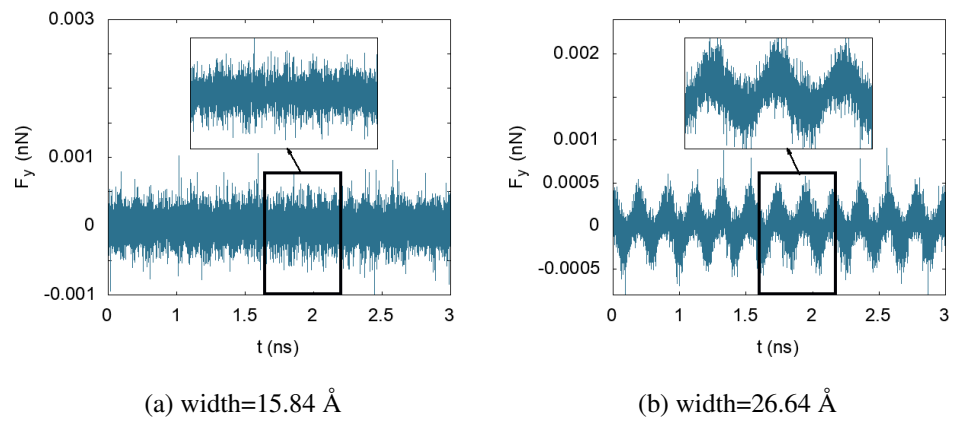


Figure 4.17: Zigzag edges of h-BN with  $v=1$  m/s

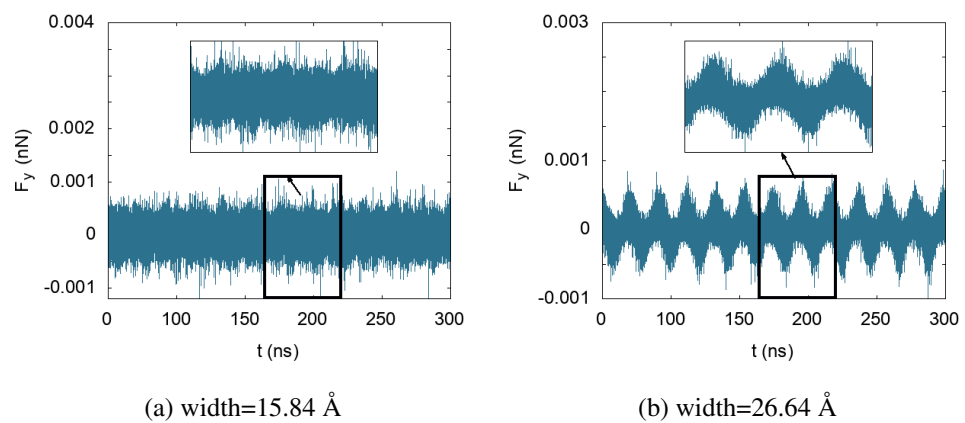


Figure 4.19: Zigzag edges of h-BN with  $v=0.01$  m/s

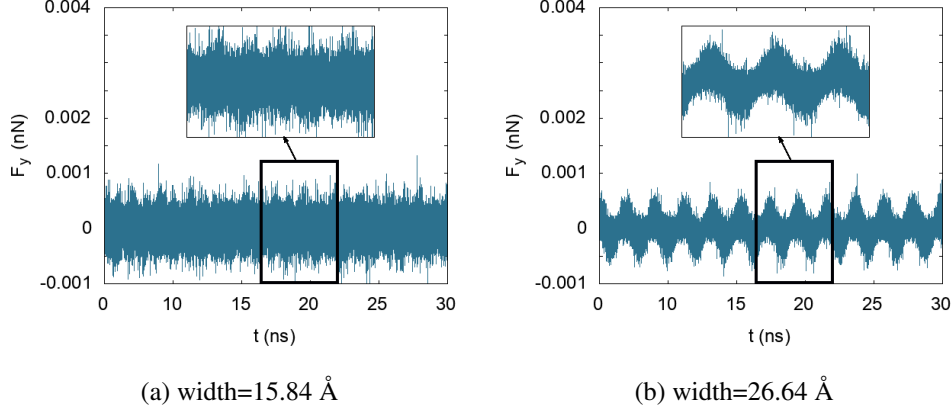


Figure 4.18: Zigzag edges of h-BN with  $v=0.1$  m/s

The frictional behavior of two different zigzag edged h-BN samples was seen to be very different from one another. In Figure.4.17, the smaller h-BN nanoribbon's (a) slide with 1 m/s  $F_y$  change between  $\pm 0.001$  Nn and the periodic motion was not observed. On the other hand, the force on the larger sample (b) fluctuated between  $\pm 0.0005$  Nn make this motion the whole sliding process. When sliding velocity decrease to 0.1 m/s in Figure.4.18,  $F_y$  increased both sample widths, and the narrower sample (a) displays a distinct periodic behavior in comparison to the faster velocity. The wider sample (b) behaves very similarly to the 1 m/s velocity. For the lowest velocity of 0.01 m/sec, zigzag edged h-BN showed different frictional behavior, where the width was 26.64 Å; was displayed the periodic motion in each velocity for complete sliding processes. However, for the larger width of 15.84 Å, we observed this motion rarely and only for slower velocities.

Table 4.4: Lateral force per area on zigzag edge h-BN

width of sample	$v=1$ m/s	$v=0.1$ m/s	$v=0.01$ m/s
15.84 Å	0.0053 nN/Å	0.0053 nN/Å	0.0053 nN/Å
26.64 Å	0.0051 nN/Å	0.0050 nN/Å	0.0050 nN/Å

The average lateral force of zigzag edged h-BN results have a similar trend to the armchair edged sample where as width and atom number increases frictional force decreases, but in zigzag edged h-BN, these difference are smaller than armchair one. This force might be caused symmetry of edge atoms since, in the zigzag sample, each

edge atoms was the same type (only B or only N atoms), but in the armchair, edge contains both types of atoms at each edge.



## CHAPTER 5

### CONCLUSIONS

In this thesis, nanotribological properties, various h-BN, and Au(111) interfaces were investigated using MD calculations.

In Chapter3, we studied the periodic h-BN/Au(111) interface, first using a small simulation cell to serve as a benchmark and then using a large enough production cell to minimize strain between the two components. We calculated the lateral forces and friction coefficients on h-BN at different velocities, temperatures, and loads. In the larger sample, we conducted all our calculations at two different thermostat frequencies to understand the effect of the interaction with the artificial heat bath. The results showed that the benchmark sample has smaller friction coefficients than the production sample, while the thermostat frequency seems to have little effect. In all calculations, the friction coefficient decreases as load increases. This appears to be a universal behavior. While the temperature changes the friction coefficient significantly, the velocity of sliding appears to have very little effect.

In Chapter4, we investigated the non-periodic mono layered boron nitride and periodic gold interface in the form of hexagonal h-BN flakes and nanoribbons. For the hexagonal nanoflakes, the sliding direction, which we varied in increments of 5 degrees from 0 to 20 degrees, has a clear effect on the friction forces. For this range of angles, the forces were seen to increase with the increasing angle with respect to the original sliding direction. As a second examination of the edge effects, we study the frictional properties of nanoribbons with zigzag and armchair edges. We include two different widths for each edge structure. The frictional forces were seen to depend very strongly on both the edge type and width. The effect of the edge type can be explained by the registry of the h-BN atoms and the underlying Au atoms. For both

edge types, the larger widths yield a smaller friction force per atom.

When we compare the friction force per atom of all the different systems studied, we encounter an interesting picture. The lateral frictional force per h-BN atom has the highest value in a production sample, the hexagonal flake results are the nearly half of the production sample, and the nanoribbons have the lowest lateral friction force at room temperature and without any load.

## REFERENCES

- [1] V. E. Ppplin, “An introduction to crystal analysis. By Sir Wm. Bragg, K.B.E., D.Sc., F.R.S. Pp. vii+168. London: G. Bell & Son, Ltd., 1928. 12s,” *Journal of the Society of Chemical Industry*, vol. 47, no. 44, pp. 1162–1163, 1928.
- [2] G. T. B.Sc., “Cvi. a molecular theory of friction,” *The London, Edinburgh, and Dublin Philosophical Magazine and Journal of Science*, vol. 7, no. 46, pp. 905–939, 1929.
- [3] F. P. Bowden and D. Tabor, “Friction, lubrication and wear: a survey of work during the last decade,” *British Journal of Applied Physics*, vol. 17, pp. 1521–1544, dec 1966.
- [4] M. Hirano and K. Shinjo, “Atomistic locking and friction,” *Phys. Rev. B*, vol. 41, pp. 11837–11851, Jun 1990.
- [5] K. Shinjo and M. Hirano, “Dynamics of friction: superlubric state,” *Surface Science Letters*, vol. 283, pp. A255–A255, Jan 1993.
- [6] M. D. Diego MARCHETTO, Tim FESER, “Microscale study of frictional properties of graphene in ultra high vacuum,” *Friction*, vol. 3, no. 2, p. 161, 2015.
- [7] S. Domínguez-Meister, T. C. Rojas, M. Brizuela, and J. C. Sánchez-López, “Solid lubricant behavior of mos2 and wse2-based nanocomposite coatings,” in *Science and technology of advanced materials*, 2017.
- [8] Y. Kimura, T. Wakabayashi, K. Okada, T. Wada, and H. Nishikawa, “Boron nitride as a lubricant additive,” *Wear*, vol. 232, no. 2, pp. 199 – 206, 1999.
- [9] S. Kawai, A. Benassi, E. Gnecco, H. Söde, R. Pawlak, X. Feng, K. Müllen, D. Passerone, C. A. Pignedoli, P. Ruffieux, R. Fasel, and E. Meyer, “Superlubricity of graphene nanoribbons on gold surfaces,” *Science*, vol. 351, no. 6276, pp. 957–961, 2016.

- [10] H. Zhang, Z. H. Fu, D. Legut, T. C. Germann, and R. F. Zhang, “Stacking stability and sliding mechanism in weakly bonded 2d transition metal carbides by van der waals force,” *RSC Adv.*, vol. 7, pp. 55912–55919, 2017.
- [11] G. Binnig, C. F. Quate, and C. Gerber, “Atomic force microscope,” *Phys. Rev. Lett.*, vol. 56, pp. 930–933, Mar 1986.
- [12] R. Bennewitz, “Friction force microscopy,” *Materials Today*, vol. 8, no. 5, pp. 42 – 48, 2005.
- [13] C. Petzold, M. Koch, and R. Bennewitz, “Friction force microscopy of tribochemistry and interfacial ageing for the siox/si/au system,” *Beilstein Journal of Nanotechnology*, vol. 9, pp. 1647–1658, 2018.
- [14] A. Ranjan, K. L. Pey, and S. J. O’Shea, “The interplay between drift and electrical measurement in conduction atomic force microscopy,” *Review of Scientific Instruments*, vol. 90, no. 7, p. 073701, 2019.
- [15] “Images of graphene and atomic force microscopy scanning.”
- [16] Y. Liu, A. Song, Z. Xu, R. Zong, J. Zhang, W. Yang, R. Wang, Y. Hu, J. Luo, and T. Ma, “Interlayer friction and superlubricity in single-crystalline contact enabled by two-dimensional flake-wrapped atomic force microscope tips,” *ACS Nano*, vol. 12, no. 8, pp. 7638–7646, 2018. PMID: 30060665.
- [17] S. Kwon, J.-H. Ko, K.-J. Jeon, Y.-H. Kim, and J. Y. Park, “Enhanced nanoscale friction on fluorinated graphene,” *Nano Letters*, vol. 12, no. 12, pp. 6043–6048, 2012. PMID: 22720882.
- [18] B. Vasić, I. Stanković, A. Matković, M. Kratzer, C. Ganser, R. Gajić, and C. Teichert, “Molecules on rails: friction anisotropy and preferential sliding directions of organic nanocrystallites on two-dimensional materials,” *Nanoscale*, vol. 10, pp. 18835–18845, 2018.
- [19] R. Shi, L. Gao, H. Lu, Q. Li, T. Ma, H. Guo, S. Du, X.-Q. Feng, S. Zhang, Y. Liu, P. Cheng, Y. zhong Hu, H. Gao, and J. Luo, “Moiré superlattice-level stick-slip instability originated from geometrically corrugated graphene on a strongly interacting substrate,” 2017.

- [20] C. Lee, Q. Li, W. Kalb, X.-Z. Liu, H. Berger, R. W. Carpick, and J. Hone, “Frictional characteristics of atomically thin sheets,” *Science*, vol. 328, no. 5974, pp. 76–80, 2010.
- [21] T. Filleter, J. L. McChesney, A. Bostwick, E. Rotenberg, K. V. Emtsev, T. Seyller, K. Horn, and R. Bennewitz, “Friction and dissipation in epitaxial graphene films,” *Phys. Rev. Lett.*, vol. 102, p. 086102, Feb 2009.
- [22] H. Ko, S. Kwan, H. W. Park, and A. Caron, “Chemical effects on the sliding friction of ag and au(111),” *Friction*, vol. 6, pp. 84–97, 2018.
- [23] F. J. Giessibl, S. Hembacher, H. Bielefeldt, and J. D. Mannhart, “Imaging silicon by atomic force microscopy with crystallographically oriented tips,” *Applied Physics A*, vol. 72, pp. S15–S17, 2001.
- [24] A. J. Weymouth, D. Meuer, P. Mutombo, T. Wutscher, M. Ondracek, P. Jelinek, and F. J. Giessibl, “Atomic structure affects the directional dependence of friction,” *Phys. Rev. Lett.*, vol. 111, p. 126103, Sep 2013.
- [25] C. Wang, W. Chen, Y. Zhang, Q. Sun, and Y. W. Jia, “Effects of vdw interaction and electric field on friction in mos<sub>2</sub>,” *Tribology Letters*, vol. 59, pp. 1–8, 2015.
- [26] G. Levita, E. Molinari, T. Polcar, and M. C. Righi, “First-principles comparative study on the interlayer adhesion and shear strength of transition-metal dichalcogenides and graphene,” *Phys. Rev. B*, vol. 92, p. 085434, Aug 2015.
- [27] G. Levita, A. Cavaleiro, E. Molinari, T. Polcar, and M. C. Righi, “Sliding properties of mos<sub>2</sub> layers: Load and interlayer orientation effects,” *The Journal of Physical Chemistry C*, vol. 118, no. 25, pp. 13809–13816, 2014.
- [28] J. Wang, J. Li, C. Li, X. Cai, W. Zhu, and Y. Jia, “Tuning the nanofriction between two graphene layers by external electric fields: A density functional theory study,” *Tribology Letters*, vol. 61, no. 1, pp. 1–6, 2016.
- [29] Y. Cheng, P. Zhu, and R. Li, “The influence of vertical vibration on nanoscale friction: A molecular dynamics simulation study,” 2018.
- [30] A. Smolyanitsky and J. P. Killgore, “Anomalous friction in suspended graphene,” *Physical Review B*, vol. 86, Sep 2012.

- [31] W. Ouyang, A. S. de Wijn, and M. Urbakh, "Atomic-scale sliding friction on a contaminated surface," *Nanoscale*, vol. 10, pp. 6375–6381, 2018.
- [32] Z. Ding, Q.-X. Pei, J.-W. Jiang, W. Huang, and Y.-W. Zhang, "Interfacial thermal conductance in graphene/mos2 heterostructures," *Carbon*, vol. 96, pp. 888 – 896, 2016.
- [33] A. Geim and K. Novoselov, "Graphene – the perfect atomic lattice," Oct 2010.
- [34] Z. Liu, "The diversity of friction behavior between bi-layer graphenes," *Nanotechnology*, vol. 25, p. 075703, jan 2014.
- [35] T. Jiang and Y. Zhu, "Measuring graphene adhesion using atomic force microscopy with a microsphere tip," *Nanoscale*, vol. 7, pp. 10760–10766, 2015.
- [36] Z. Ding, Q.-X. Pei, J.-W. Jiang, W. Huang, and Y.-W. Zhang, "Interfacial thermal conductance in graphene/mos2 heterostructures," *Carbon*, vol. 96, pp. 888 – 896, 2016.
- [37] W. B. Esq., "Xlvi. observations on the formation of compounds of boron and silicon with nitrogen and certain metals," *The London, Edinburgh, and Dublin Philosophical Magazine and Journal of Science*, vol. 21, no. 138, pp. 270–277, 1842.
- [38] A. Pakdel, Y. Bando, and D. Golberg, "Nano boron nitride flatland," *Chem. Soc. Rev.*, vol. 43, pp. 934–959, 2014.
- [39] R. Arenal and A. Lopez-Bezanilla, "Boron nitride materials: an overview from 0d to 3d (nano)structures," *WIREs Computational Molecular Science*, vol. 5, no. 4, pp. 299–309, 2015.
- [40] J. H. Kim, T. V. Pham, J. H. Hwang, C. S. Kim, and M. J. Kim, "Boron nitride nanotubes: synthesis and applications," *Nano Convergence*, vol. 5, p. 17, Jun 2018.
- [41] A. Merlo, V. R. S. S. Mokkalapati, S. Pandit, and I. Mijakovic, "Boron nitride nanomaterials: biocompatibility and bio-applications," *Biomater. Sci.*, vol. 6, pp. 2298–2311, 2018.

- [42] M. B. Jakubinek, B. Ashrafi, Y. Martinez-Rubi, J. Guan, M. Rahmat, K. S. Kim, S. Dénomée, C. T. Kingston, and B. Simard, “Chapter 5 - boron nitride nanotube composites and applications,” in *Nanotube Superfiber Materials (Second Edition)* (M. J. Schulz, V. Shanov, Z. Yin, and M. Cahay, eds.), Micro and Nano Technologies, pp. 91 – 111, William Andrew Publishing, second edition ed., 2019.
- [43] C. Lee, X. Wei, Q. Li, R. Carpick, J. W. Kysar, and J. Hone, “Elastic and frictional properties of graphene,” *physica status solidi (b)*, vol. 246, no. 11-12, pp. 2562–2567, 2009.
- [44] L. H. Li, J. Cervenka, K. Watanabe, T. Taniguchi, and Y. Chen, “Strong oxidation resistance of atomically thin boron nitride nanosheets,” *ACS Nano*, vol. 8, no. 2, pp. 1457–1462, 2014. PMID: 24400990.
- [45] Q. Cai, A. Du, G. Gao, S. Mateti, B. C. Cowie, D. Qian, S. Zhang, Y. Lu, L. Fu, T. Taniguchi, *et al.*, “Molecule-induced conformational change in boron nitride nanosheets with enhanced surface adsorption,” *Advanced Functional Materials*, vol. 26, no. 45, pp. 8202–8210, 2016.
- [46] L. Liu, M. Zhou, L. Jin, L. Li, Y. Mo, G. Su, X. Li, H. Zhu, and Y. Tian, “Recent advances in friction and lubrication of graphene and other 2d materials: Mechanisms and applications,” *Friction*, vol. 7, no. 3, pp. 199–216, 2019.
- [47] D. Frenkel and B. Smit, eds., *Understanding Molecular Simulation: From Algorithms to Applications*. Orlando, FL, USA: Academic Press, Inc., 1st ed., 1996.
- [48] L. Verlet, “Computer "experiments" on classical fluids. i. thermodynamical properties of lennard-jones molecules,” *Phys. Rev.*, vol. 159, pp. 98–103, Jul 1967.
- [49] S. Plimpton, “Fast parallel algorithms for short-range molecular dynamics,” *J. Comput. Phys.*, vol. 117, pp. 1–19, Mar. 1995.
- [50] D. Beeman, “Some multistep methods for use in molecular dynamics calculations,” *Journal of computational physics*, vol. 20, no. 2, pp. 130–139, 1976.

- [51] W. C. Swope, H. C. Andersen, P. H. Berens, and K. R. Wilson, "A computer simulation method for the calculation of equilibrium constants for the formation of physical clusters of molecules: Application to small water clusters," *The Journal of Chemical Physics*, vol. 76, no. 1, pp. 637–649, 1982.
- [52] J. E. Jones and S. Chapman, "On the determination of molecular fields. &#x2014;i. from the variation of the viscosity of a gas with temperature," *Proceedings of the Royal Society of London. Series A, Containing Papers of a Mathematical and Physical Character*, vol. 106, no. 738, pp. 441–462, 1924.
- [53] J. E. Jones and S. Chapman, "On the determination of molecular fields. &#x2014;ii. from the equation of state of a gas," *Proceedings of the Royal Society of London. Series A, Containing Papers of a Mathematical and Physical Character*, vol. 106, no. 738, pp. 463–477, 1924.
- [54] P. M. Morse, "Diatomic molecules according to the wave mechanics. ii. vibrational levels," *Physical Review*, vol. 34, no. 1, p. 57, 1929.
- [55] M. S. Daw and M. I. Baskes, "Semiempirical, quantum mechanical calculation of hydrogen embrittlement in metals," *Phys. Rev. Lett.*, vol. 50, pp. 1285–1288, Apr 1983.
- [56] M. S. Daw and M. I. Baskes, "Embedded-atom method: Derivation and application to impurities, surfaces, and other defects in metals," *Phys. Rev. B*, vol. 29, pp. 6443–6453, Jun 1984.
- [57] M. I. Baskes, "Modified embedded-atom potentials for cubic materials and impurities," *Physical review B*, vol. 46, no. 5, p. 2727, 1992.
- [58] M. Finnis and J. Sinclair, "A simple empirical n-body potential for transition metals," *Philosophical Magazine A*, vol. 50, no. 1, pp. 45–55, 1984.
- [59] A. Horsfield, A. Bratkovsky, M. Fearn, D. Pettifor, and M. Aoki, "Bond-order potentials: Theory and implementation," *Physical Review B*, vol. 53, no. 19, p. 12694, 1996.
- [60] A. C. Van Duin, S. Dasgupta, F. Lorant, and W. A. Goddard, "Reaxff: a reactive force field for hydrocarbons," *The Journal of Physical Chemistry A*, vol. 105, no. 41, pp. 9396–9409, 2001.

- [61] F. H. Stillinger and T. A. Weber, “Computer simulation of local order in condensed phases of silicon,” *Physical review B*, vol. 31, no. 8, p. 5262, 1985.
- [62] F. o. C. Eni Generalic and Technology, “Chemistry glossary,” Oct 2018.
- [63] A. K. Rappé, C. J. Casewit, K. S. Colwell, W. A. Goddard, and W. M. Skiff, “Uff, a full periodic table force field for molecular mechanics and molecular dynamics simulations,” 1992.
- [64] H. A. Lorentz, “Ueber die anwendung des satzes vom virial in der kinetischen theorie der gase,” *Annalen der Physik*, vol. 248, no. 1, pp. 127–136, 1881.
- [65] D. Berthelot, “Sur le mélange des gaz,” *Compt. Rendus*, vol. 126, pp. 1703–1706, 1898.
- [66] J. Tersoff, “Empirical interatomic potential for carbon, with applications to amorphous carbon,” *Phys. Rev. Lett.*, vol. 61, pp. 2879–2882, Dec 1988.
- [67] A. Kinac ı, J. B. Haskins, C. Sevik, and T. Çağ ın, “Thermal conductivity of bn-c nanostructures,” *Phys. Rev. B*, vol. 86, p. 115410, Sep 2012.
- [68] R. G. Parr, “Density functional theory of atoms and molecules,” in *Horizons of Quantum Chemistry*, pp. 5–15, Springer, 1980.
- [69] P. H. Hünenberger and P. Chemie, “Thermostat algorithms for molecular dynamics simulations,” 2005.
- [70] S. Nosé, “A molecular dynamics method for simulations in the canonical ensemble,” *Molecular Physics*, vol. 52, no. 2, pp. 255–268, 1984.
- [71] W. G. Hoover, “Canonical dynamics: Equilibrium phase-space distributions,” *Phys. Rev. A*, vol. 31, pp. 1695–1697, Mar 1985.
- [72] H. J. C. Berendsen, J. P. M. Postma, W. F. van Gunsteren, A. DiNola, and J. R. Haak, “Molecular dynamics with coupling to an external bath,” *The Journal of Chemical Physics*, vol. 81, no. 8, pp. 3684–3690, 1984.
- [73] W. Tyson and W. Miller, “Surface free energies of solid metals: Estimation from liquid surface tension measurements,” *Surface Science*, vol. 62, no. 1, pp. 267 – 276, 1977.

- [74] M. Baksi, D. Toffoli, O. Gulseren, and H. Ustunel, “Nanotribological properties of the h-bn/au (111) interface: A dft study,” *The Journal of Physical Chemistry C*, vol. 123, no. 46, pp. 28411–28418, 2019.